



universität
wien

MASTERARBEIT / MASTER'S THESIS

Titel der Masterarbeit / Title of the Master's Thesis

**„The radiative impact of clouds on idealized
extratropical cyclones“**

verfasst von / submitted by

Klara Kornelia Butz, BSc BSc

angestrebter akademischer Grad / in partial fulfilment of the requirements for the degree of

Master of Science (MSc)

Wien, 2022 / Vienna, 2022

Studienkennzahl lt. Studienblatt /
degree programme code as it appears on
the student record sheet:

A 066 614

Studienrichtung lt. Studienblatt /
degree programme as it appears on
the student record sheet:

Master's degree programme Meteorology

Betreut von / Supervisor:

Univ.-Prof. Dr. Aiko Voigt

Zusammenfassung

Außertropische Zyklone steuern das tägliche Wetter in den mittleren Breiten. Diese Zyklone werden durch diabatische Prozesse wie latentes Heizen oder kurz- und langwellige Strahlung beeinflusst. Der Einfluss von Strahlungsprozessen, insbesondere jener der Wolkenstrahlung, auf die Entwicklung außertropischer Zyklone wurde bisher jedoch kaum untersucht. Durch Simulationen idealisierter barokliner Lebenszyklen mit dem globalen Atmosphärenmodell ICON-NWP in einem Aquaplaneten-Setup mit vorgeschriebenen Meeresoberflächentemperaturen untersuche ich den Einfluss des Wolkenstrahlungsheizens auf außertropische Zyklone. Ich verwende sechs verschiedene Simulationen, um nicht nur den Gesamteinfluss des Wolkenstrahlungsheizens zu erforschen, sondern auch, um die Auswirkungen von isoliertem Wolkenstrahlungsheizen in der planetaren Grenzschicht und der freien Troposphäre zu charakterisieren. Dies erreiche ich, indem ich das Wolkenstrahlungsheizen des Modells unterhalb oder oberhalb einer bestimmten Höhe auf null setze, bevor sie an den dynamischen Kern weitergegeben wird. Um die Robustheit der Ergebnisse zu testen, vergleiche ich die Auswirkungen des Wolkenstrahlungsheizens zwischen den Modellversionen ICON 2.1 und 2.6. Wenn das Strahlungsschema ausgeschaltet ist, erzeugen beide Modellversionen ähnliche Zyklone. Die Aktivierung des Wolkenstrahlungsheizens führt zu gegensätzlichen Auswirkungen auf die Zyklone. ICON 2.1 zeigt eine Abschwächung der Zyklone durch Wolkenstrahlungsheizen, während ICON 2.6 stärkere Zyklone erzeugt, wenn Wolkenstrahlungsheizen aktiv ist. Die Spitzenwerte der Eddy-kinetischen Energie (EKE) auf 300 hPa werden durch Wolkenstrahlungsheizen in ICON 2.1 um bis zu 11% gedämpft. In ICON 2.6 erhöht Wolkenstrahlungsheizen den Spitzenwert der EKE bei 300 hPa um bis zu 7%. Eine weitere Analyse zeigt, dass Wolken in der Grenzschicht eine stark abschwächende Wirkung haben und Wolken in der freien Troposphäre die Zyklone in beiden Modellversionen stärken. Da die ICON 2.1-Simulationen mehr tief liegende Wolken erzeugen, dominiert die abschwächende Wirkung. Tiefliegende Wolken sind in ICON 2.6 weniger stark ausgeprägt, was zu einer allgemeinen Verstärkung der Zyklone führt. Die sich daraus ergebende Auswirkung des Wolkenstrahlungsheizens hängt also von der vertikalen Verteilung der Wolken ab. Diese neuen Erkenntnisse unterstreichen die Bedeutung des Wolkenstrahlungsheizens für die Zyklonendynamik. In dieser Studie zeige ich, wie Unterschiede in der Verteilung von Wolken und ihre Strahlungseffekte zu unterschiedlichen Entwicklungen der Zyklone führen. Weitere Untersuchungen anhand von idealisierten und realistischen Fallstudien sind erforderlich, um ein dynamisches Verständnis für die Auswirkungen des Wolkenstrahlungsheizens von niedrigen und hohen Wolken auf Zyklone zu erlangen.

Abstract

Extratropical cyclones are the main driver of everyday weather in the mid-latitudes. These cyclones are affected by diabatic processes such as latent heating and radiation. However, the impact of radiative processes, especially cloud-radiation interaction, on the evolution of extratropical cyclones has hardly been investigated so far. By performing idealized baroclinic life cycle simulations with the global atmosphere model ICON-NWP in an aqua-planet setup with prescribed sea surface temperatures, I study the impact of cloud-radiative heating (CRH) on extratropical cyclones. Six different simulation setups are used to not only isolate the overall impact of CRH but also to distinguish the impact of isolated CRH in the boundary layer and free troposphere. This is achieved by setting the model's cloud-radiative heating below or above a certain altitude to zero before passing them to the dynamical core. To test the robustness of the results, the CRH impact is compared between model versions ICON 2.1 and 2.6. When the radiation scheme is turned off, both model versions produce similar cyclones. Enabling cloud-radiative heating leads to contradicting impacts on the cyclones. ICON 2.1 shows cyclone weakening due to CRH, while ICON 2.6 produces stronger cyclones when CRH is active. Peak eddy kinetic energy (EKE) at 300 hPa is damped by up to 11% due to CRH in ICON 2.1. In ICON 2.6, CRH increases peak EKE at 300 hPa by up to 7%. Further analysis shows that low-level clouds have a robust weakening impact, and high-level clouds strengthen the cyclone in both model versions. Since ICON 2.1 simulations produce more low-level clouds, the weakening impact dominates. Low-level clouds are less pronounced in ICON 2.6, leading to an overall strengthening of the cyclone. The resulting CRH impact, therefore, depends on the vertical distribution of clouds. These new insights highlight the importance of CRH for cyclone dynamics. In this study, I show how the differences in the distribution of clouds and their radiative effects result in different cyclone evolution. Further studies via idealized and real case studies are required to gain a dynamical understanding of the CRH impact on cyclones from low-level and high-level clouds.

Contents

Zusammenfassung	1
Abstract	2
Acronyms	5
1 Introduction	6
1.1 Extratropical cyclones	7
1.2 Diabatic processes and energy transformation	13
1.3 Cloud-radiation interaction in extratropical cyclones	17
2 Research questions	22
3 Methods	23
3.1 Baroclinic life cycles	23
3.2 ICON model and model setup	26
3.3 Simulations	28
3.4 Analysis methods	29
4 Results	34
4.1 Reproducing the results of Schäfer and Voigt (2018) with ICON 2.1	34
4.2 Isolating the impact of cloud-radiative heating with a new simulation approach	37
4.3 Changes in the cloud-radiative heating impact with a new model version . .	38
4.4 Differences in clouds and radiative heating rates in the same large-scale envi- ronment	41
4.5 Competing impacts of clouds in the boundary layer and free troposphere . .	43
5 Conclusion	51
Bibliography	55
List of Figures	60
Acknowledgments	62

Acronyms

ACRE	Atmospheric cloud-radiative effect
APE	Available potential energy
CRE	Cloud-radiative effect
CRH	Cloud-radiative heating
EAPE	Eddy available potential energy
EKE	Eddy kinetic energy
ETC	Extratropical cyclone
HLRE-3	High Performance Computing system for Earth system research
LC1	Baroclinic life cycle type 1
LC2	Baroclinic life cycle type 2
MAPE	Zonal mean moist available potential energy
NWP	Numerical weather prediction
PV	Potential vorticity
QGPV	Quasi-geostrophic potential vorticity
RRTM	Rapid Radiative Transfer Model
SST	Sea surface temperature
TOA	Top of atmosphere
ZAPE	Zonal mean available potential energy
ZKE	Zonal mean kinetic energy

1 | Introduction

Extratropical cyclones (ETCs) are the prime driver of daily weather in the mid-latitudes. They transport energy and moisture and are responsible for up to 90% of precipitation (Catto et al., 2012). Due to their relevance for everyday life, ETCs are important study objects, and in order to forecast ETCs as accurately as possible, we need to understand their dynamics, life cycles, and features.

ETCs are strongly influenced by diabatic processes, such as latent heating, friction, and radiation (Stoelinga, 1996). Latent heat release leads to stronger cyclones (Zimmerman et al., 1989; Booth et al., 2013b) and has been a prominent subject of ETCs studies for several decades. Radiation was often neglected in studies to focus on processes such as latent heating (Boutle et al., 2011; Booth et al., 2013b). Chagnon et al. (2013), however, found that longwave radiation is an important contributor to positive potential vorticity (PV) anomalies in the upper troposphere and Grise et al. (2019) found cloud radiation to dampen extratropical storm track intensity. Schäfer and Voigt (2018) used idealized baroclinic life cycle simulations with different radiation settings and concluded that radiative heating weakens the idealized cyclone. Moreover, they suggest that cloud-radiative heating (CRH) can contribute considerably to the weakening impact. Although radiative heating rates are smaller than those from latent heating, the radiative impact is due to the fact that radiation acts during the whole life of a cloud, whereas latent heating occurs predominantly during cloud formation.

A full dynamical picture on CRH in ETCs is still missing. Using improved simulation strategies, I pick up on the results by Schäfer and Voigt (2018) and investigate the impact of CRH in more detail. The baroclinic life cycle simulations are performed in the global atmosphere model ICON-NWP in an aquaplanet setup with prescribed sea surface temperatures (SSTs). To make statements about the robustness of the results by Schäfer and Voigt (2018), I use the two ICON model versions 2.1 and 2.6. ICON 2.6 is the current version in operational use. For each model version, I apply 6 different radiation settings. The new simulation strategies allow for isolating the impact of CRH while avoiding changes in the mean state due to clear-sky radiative cooling. This improvement to the original setup by Schäfer and Voigt (2018) allows for a clearer understanding of the CRH impact on the cyclone. I am particularly dedicated to the question of how clouds in different altitudes impact ETCs via

their radiative heating. The new modeling approach also allows me to isolate the impact of low-level and upper-level CRH by constraining CRH in the simulations at different altitudes.

Starting by presenting the theoretical background on ETCs and their interaction with clouds, I then explain the methodology of baroclinic life cycle simulations and all radiation settings used in this thesis. The result section shows how CRH affects cyclone strength and uncovers important findings on the role of CRH for the cyclone dynamics.

1.1 Extratropical cyclones

For understanding the evolution and features of ETCs, the two most established concepts are the Norwegian model (Bjerknes, 1922) and the Shapiro-Keyser model (Shapiro and Keyser, 1990), depicted in Figure 1.1. Even though both models are not exactly applicable to every ETC, they explain the most important features of ETCs. Therefore, both conceptual models should be considered for understanding ETCs (see Cotton et al., 2011). In the Norwegian model, cyclones develop along the polar front, which is defined as a sharp meridional temperature gradient. A perturbation then evolves into a frontal system of low pressure, and the cyclone deepens. As soon as the warm sector is caught up by the cold sector behind, an occlusion forms. The occluded front then marks the new polar front, where a new cyclone can begin to form (Bjerknes, 1922). However, many observed and idealized ETCs do not resemble this concept, questioning its universal application (e.g. Hoskins and West, 1979).

Shapiro and Keyser (1990) developed a new concept in the late 20th century, where the fronts fracture at the cyclone center. The fronts amplify and the cold and warm fronts form a “T-bone” structure. During this process, warm air becomes isolated in the cyclone’s center - forming a warm seclusion.

Conveyor belts

The following explanations on major air circulations associated with ETCs are based on chapter 9 of Siebesma et al. (2020). The described flow is located on the Northern Hemisphere. Flows on the Southern Hemisphere are organized analogously.

According to the conveyor belt model, an ETC’s low-pressure center is surrounded by various circulations, the conveyor belts (Figure 1.2). The warm conveyor belt transports warm, moist air from the surface to higher altitudes. Due to the high amount of moisture, this circulation tends to be convectively unstable and convective clouds are embedded within them, often accompanied by heavy precipitation. The warm conveyor belt is located ahead of the cold front, flowing poleward and ascending above the warm front. During the ascent, stratiform clouds and precipitation are formed, creating strong precipitation before the warm front passes through. At higher altitudes, the warm conveyor belt starts to move

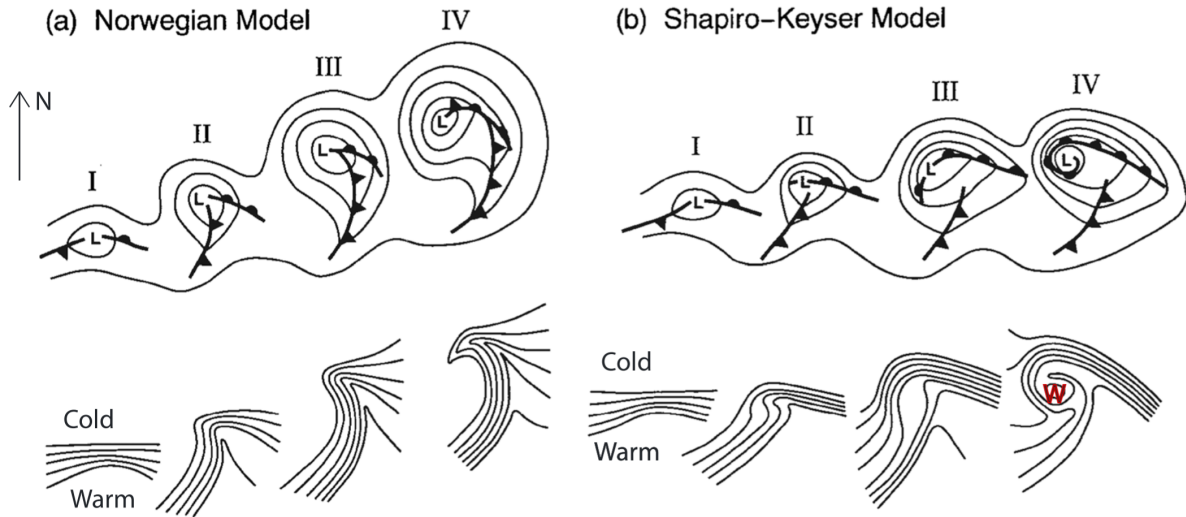


Figure 1.1: Two conceptual models on ETC evolution. The top row shows geopotential height in the lower troposphere including cold and warm fronts. The lower row depicts potential temperature in the lower troposphere. a) The Norwegian model. The warm sector narrows in II and III, building an occlusion in IV, which is marked by neighboring triangles and semicircles. In the b) Shapiro-Keyser model, warm air gets trapped in the cyclone center, forming a seclusion with a frontal T-bone. Figure taken from Schultz et al. (1998).

eastward due to the strong westerlies in the upper troposphere in the mid-latitudes, creating cirrostratus and cirrus clouds, known as the typical signs of an incoming warm front.

As the name of the dry conveyor belt already suggests, it consists of very dry air originating in upper tropospheric levels descending equatorward of the surface low. The air from the dry conveyor belt is typically very cold and corresponds to the known cold air advection behind a cold front.

The third major air circulation, the cold conveyor belt, flows from north-eastern regions towards the minimum pressure, moving parallel to the northern edge of the warm front and streaming beneath the warm conveyor belt. Warm precipitation of the warm conveyor belt moistens the cold flow, leading to stratus clouds and rising motions as the cold conveyor belt approaches the minimum pressure center. It splits into two branches, where one is deflected to the east, finally being aligned with the warm conveyor belt but at lower altitudes. The second one is circulating the surface low cyclonically, creating the typical comma-shaped clouds located west to the pressure center.

An example of an ETC's frontal structure and precipitation retrieved by satellite observations is shown in Figure 1.3. Posselt et al. (2008) observed a decaying ETC southwest of Iceland on 22.11.2006 at around 06:00 UTC. Ahead of the cyclone (approximately at 40°N - 42°N) are cirrus and cirrostratus clouds, emerging from nimbostratus clouds in the frontal zone. Cumulus clouds are located behind the front. The strongest precipitation rates are located in the rear frontal zone, given by CloudSat estimates. Only light precipitation rates

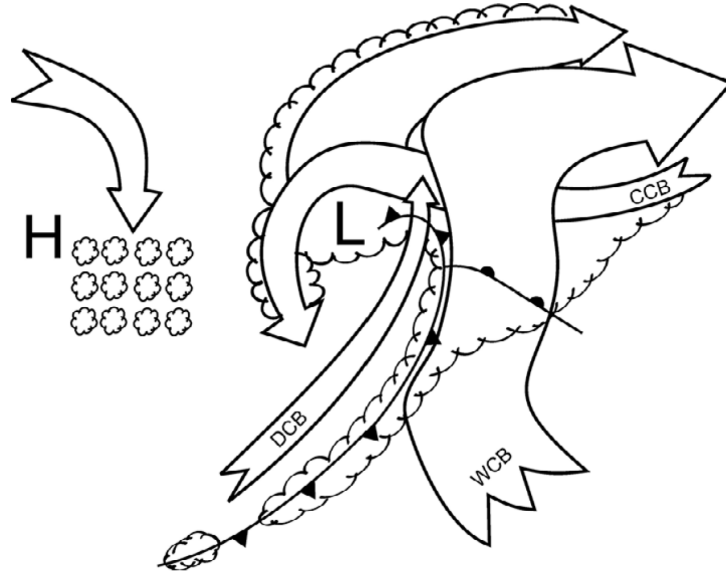


Figure 1.2: Conceptual view on the conveyor belt model for an ETC on the Northern Hemisphere. H and L mark the centers of high and low pressure, respectively. The three conveyor belt circulations are the warm conveyor belt (WCB), the cold conveyor belt (CCB), and the dry conveyor belt (DCB). The positions of the cold and warm fronts are given by the lines with triangles and semicircles, respectively. From Siebesma et al. (2020).

are detected ahead of the front.

Baroclinic instability

Baroclinic instability is a key mechanism for the development of mid-latitude synoptic waves. The following explanation uses the simplifications of quasi-geostrophic theory, which provides a theoretical basis for understanding how ETCs develop (Holton, 2004, p. 228).

The base state of a baroclinic instability is a stably stratified, rotating fluid that has decreasing temperature and increasing density towards the poles. The horizontal temperature gradient requires vertical wind shear of the base flow to increase with height. The instability grows by releasing potential energy associated with the temperature gradient. The growing perturbation consists of two waves amplifying each other: A quasi-geostrophic potential vorticity (QGPV) anomaly at higher levels sets a surface temperature anomaly into motion, which then interacts and amplifies the upper-level QGPV anomaly (see Swanson, 2003, p. 43ff). A schematic picture of this process is shown in Figure 1.4.

Whether a QGPV anomaly at altitude D and of length L grows is dependent on its "deformation depth" $f_0 L / N$, where f_0 is the constant Coriolis parameter and N is the Brunt-Väisälä frequency. If $L \ll ND / f_0$, surface and QGPV dynamics will not be coupled and the perturbation will not grow. A persisting perturbation must therefore be either short-waved and shallow or long-waved and deep (see Swanson, 2003, p. 45f).

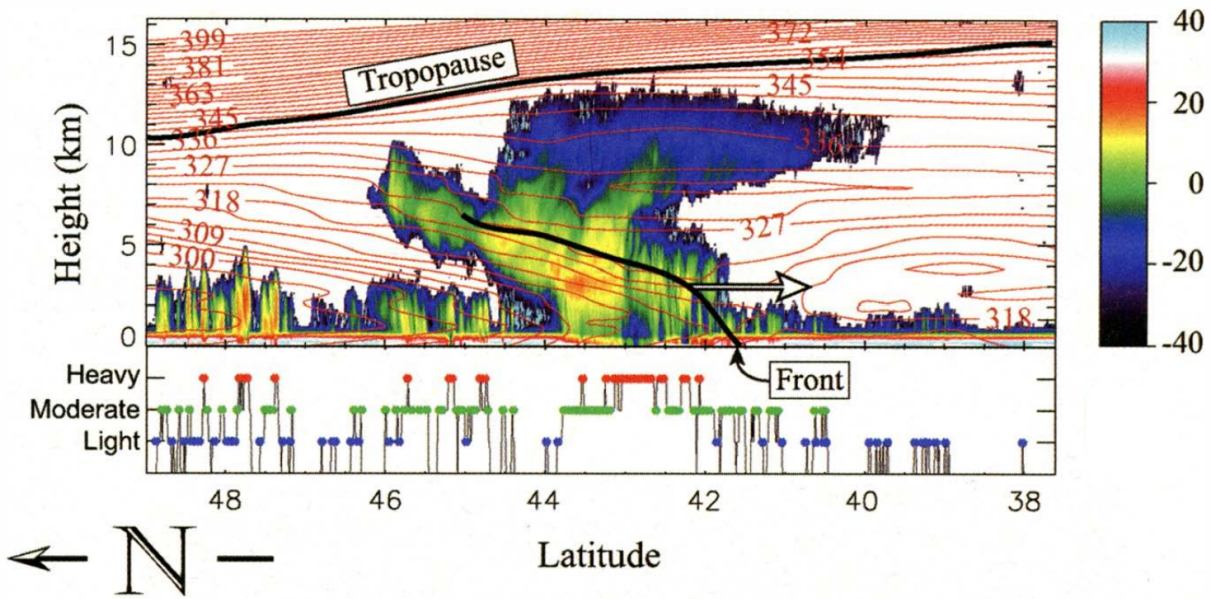


Figure 1.3: Radar reflectivity (in dBZ, color shadings) of a North Atlantic baroclinic storm observed with CloudSat on 22.11.2006 southwest of Iceland, shown as a cross section. The red contours show equivalent potential temperature in K (ECMWF-analyzed), the black lines mark the position of the tropopause and of the front. The lower diagram shows CloudSat-estimated precipitation rates. Figure taken from Posselt et al. (2008). Copyright © 2008 American Meteorological Society

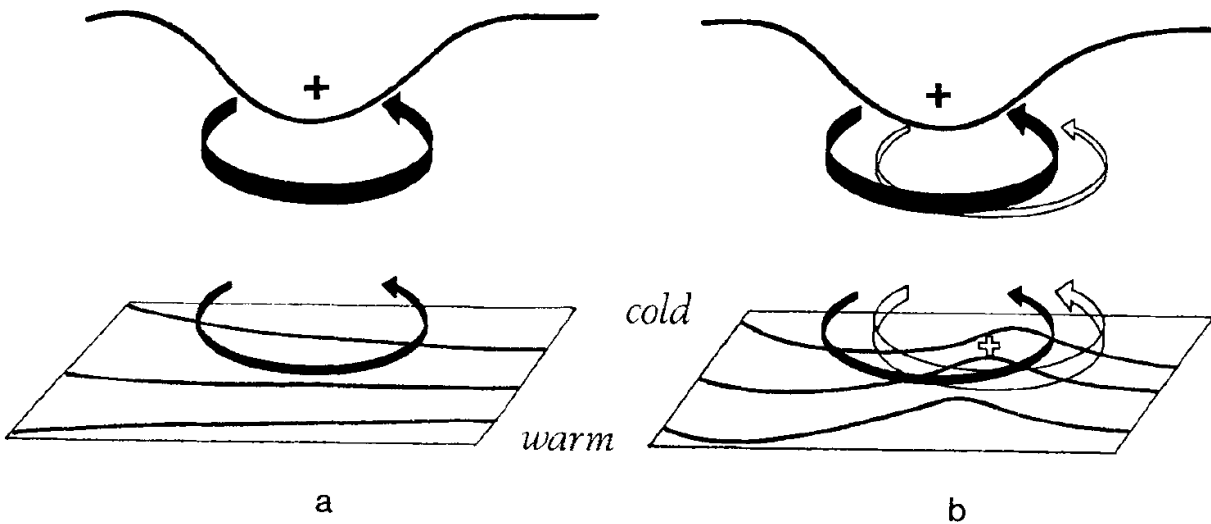


Figure 1.4: A schematic view on cyclogenesis due to a) an upper-level PV anomaly over a low-level baroclinicity. The PV anomaly is marked by a solid plus sign, temperature is shown by the contours at the surface. At low levels, the induced circulation is denoted by the arrow. b) The circulation leads to advection of warm air, creating a warm air anomaly marked by the open arrow at the surface. This induces another upper-level PV anomaly, indicated by the open arrow at upper levels. Figure taken from Hoskins et al. (1985).

A first-order approximation to the baroclinic instability is the Eady model (Eady, 1949). Eady assumed a constant Coriolis parameter, constant zonal wind shear, and neglected density fluctuations in a quasi-geostrophic atmosphere. The model has "rigid lids" at the surface and the top of the proposed atmosphere. A Rossby wave at surface level propagates to the East, and another one at the upper boundary is propagating to the West. Cold surface air is associated with high pressure, therefore anticyclonic flow - and corresponds to a negative QGPV perturbation. Warm air at the surface is accompanied by low pressure and cyclonic flow and is the analogy to positive QGPV perturbations. If the deformation depth is approximately as large as the distance between the boundaries, the wave of one boundary can amplify the wave at the other boundary and baroclinic instabilities grow (see Swanson, 2003, p. 46f).

The properties of the wave corresponding to the most unstable mode, thus the fastest-growing perturbation, are depicted in Figure 1.5. In the shown case, the zonal wavenumber equals the meridional wavenumber. Figure 1.5a, d sketch the connection of potential temperature and geopotential height as described above. The trough and ridge axes of baroclinic waves are tilted westward with height, allowing temperature and wind perturbations to be partly in phase at the respective boundary. By that constellation, heat is transported poleward or equatorward.

Figure 1.5b shows the overturning circulation in the x-z plane, which is marked by the ageostrophic stream function. Warm and cold air mass axes are sloping eastward, marked by L and W in Figure 1.5c. East of the trough, there is a negative temperature perturbation and, concurrently, ascent in the vertical. An air parcel in this region cools adiabatically, creating the typical "comma clouds" of surface troughs (Swanson, 2003, p. 46ff).

Quasi-geostrophic theory is based on the dry atmosphere and cannot consider the role of diabatic processes for the dynamics of an ETC. It also assumes only small perturbations, whereas perturbations in the real atmosphere are usually larger. To describe atmospheric circulation and understand the role of diabatic processes, Hoskins et al. (1985) developed the concept "PV thinking". PV is a conserved quantity in an adiabatic, frictionless fluid. Therefore, its temporal derivative can be predicted by advection. PV can be also created or destroyed by diabatic processes. Since PV is conserved in an adiabatic and frictionless flow, it can be used to trace the impact of diabatic processes on the circulation (Chagnon et al., 2013). PV is also used to mark the dynamical tropopause, which is mostly defined by the value of 2 PVU (potential vorticity units). PV is lower than 2 PVU in the troposphere and higher in the stratosphere (Catto, 2016).

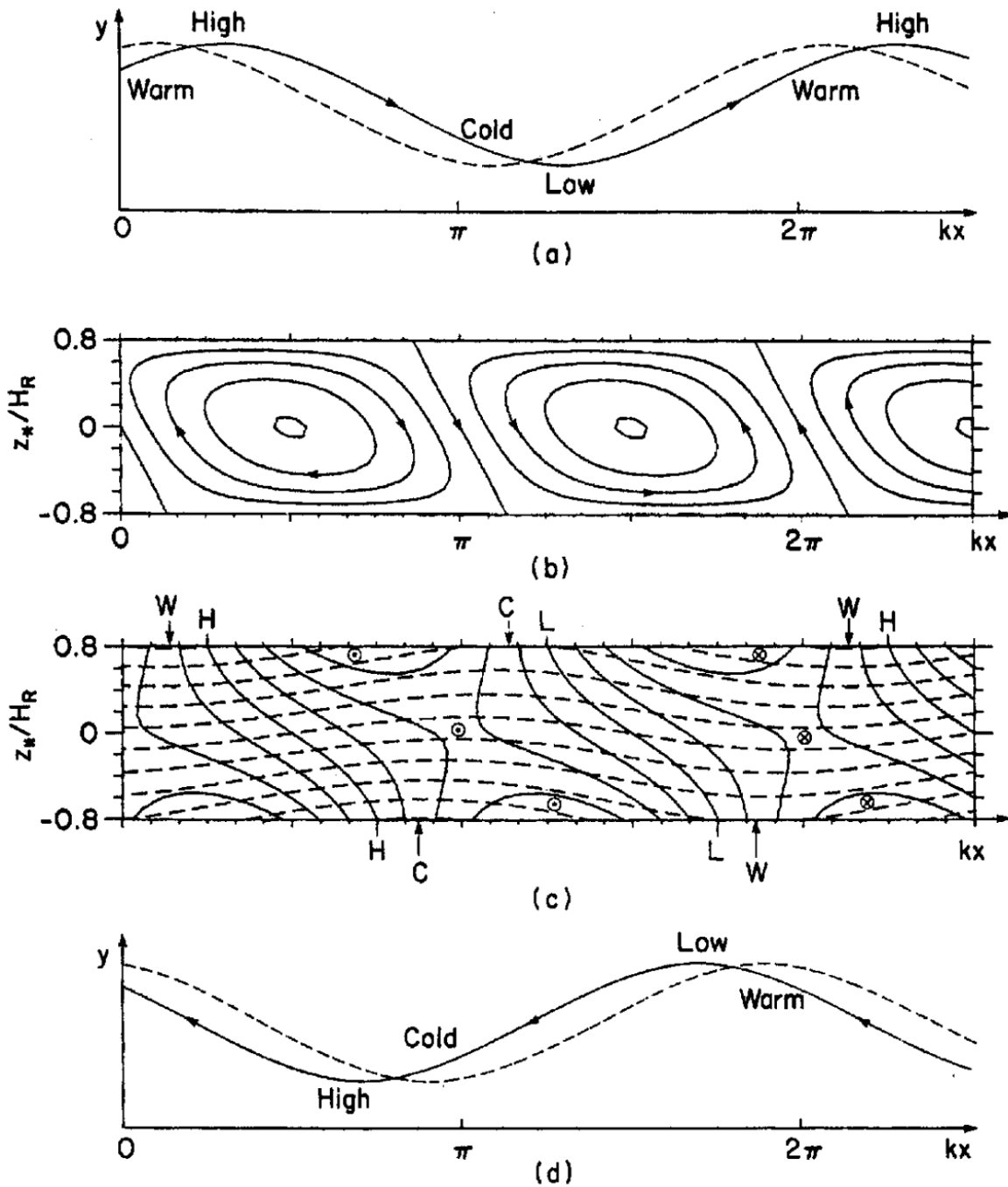


Figure 1.5: The most unstable Eady wave. a) An isobar (solid line) and an isotherm (dashed line) at the upper boundary. b) The overturning in the x - z plane is shown by the stream function for ageostrophic flow. Ascent is located east of the surface trough, west to the surface ridge is descent. c) Meridional geostrophic wind (solid lines) and potential temperature (dashed lines) in the x - z plane. Circles with dots inside mark the axis of maximum flow towards the pole, and circles with crosses indicate the axis of maximum flow towards the equator. Ridge and trough axes are marked by H (high) and L (low) and the phase of warmest/coldest air is indicated by W and C, respectively. d) An isobar (solid line) and an isotherm (dashed line) at the lower boundary. The pattern is similar to the one at the upper boundary but phase-shifted to the east relative to the isobars. Figure taken from Gill (1982).

1.2 Diabatic processes and energy transformation

The evolution of an ETC is strongly affected by diabatic processes, such as latent heat release, radiative cooling or warming, diffusion, and dissipation. The process affecting the ETC the strongest is latent heat release, which is related to cloud-microphysical processes and convection. Diabatic processes were shown to contribute strongly to cyclone pressure deepening (Fink et al., 2012).

From a "PV thinking" perspective, latent heating enhances the coupling between surface and upper-level waves by generating a positive low-level PV anomaly (Stoelinga, 1996). If the initial relative humidity is particularly high, the ascending air in the cyclone will saturate soon. Around the cyclone center, diabatic heating is therefore increased. This leads to a stronger vertical gradient of diabatic heating, creating the positive PV anomaly in the lower troposphere. At upper levels, a negative PV anomaly is generated, which stems from adiabatic PV advection from the stratosphere. The low-level PV anomaly can additionally intensify the upper-level anomaly by the associated cyclonic wind field or weaken the upper-level anomaly by diabatic PV erosion. These effects tilt the PV axis westward, leading to further intensification (see Büeler and Pfahl, 2017).

Some studies investigated the impact of surface friction, finding that cutting surface friction from a simulated ETC strengthens the ETC. This is connected to an indirect intensification of the PV anomaly at upper levels and, due to thermal diffusion in the cyclone's warm sector, to the generation of low-level PV (Stoelinga, 1996).

Diabatic impacts on PV act in different regions of the ETC, varying from process to process. A case study by Spreitzer et al. (2019), focusing on an ETC in the North Atlantic around 6 February 2017, showed the contribution of the large-scale cloud scheme, convection, turbulence, and radiation on the cyclone's PV (Figure 1.6).

Together, large-scale cloud processes and convection enhance upper-tropospheric negative PV (Figure 1.6a, b), which is consistent with the findings of Stoelinga (1996).

Turbulence, on the other hand, has large amounts of negative PV above the tropopause (Figure 1.6c), playing a key role in the erosion of the tropopause. Furthermore, the PV in the cold front is reduced by turbulence, while turbulence enhances PV in the warm front.

In contrast to turbulent PV modification, radiation is a relatively slow process. Due to its more homogeneous impact on large areas, radiation can have large contributions to the average PV budget, especially over longer time scales. Radiative PV modification is more pronounced in low-tropopause regions (Figure 1.6d), because radiative cooling depends largely on clouds and moisture gradients. Together with convection, it can produce vertical PV modification dipoles, influencing the propagation of Rossby waves.

The impact of diabatic processes on ETCs can also be studied by means of idealized modeling.

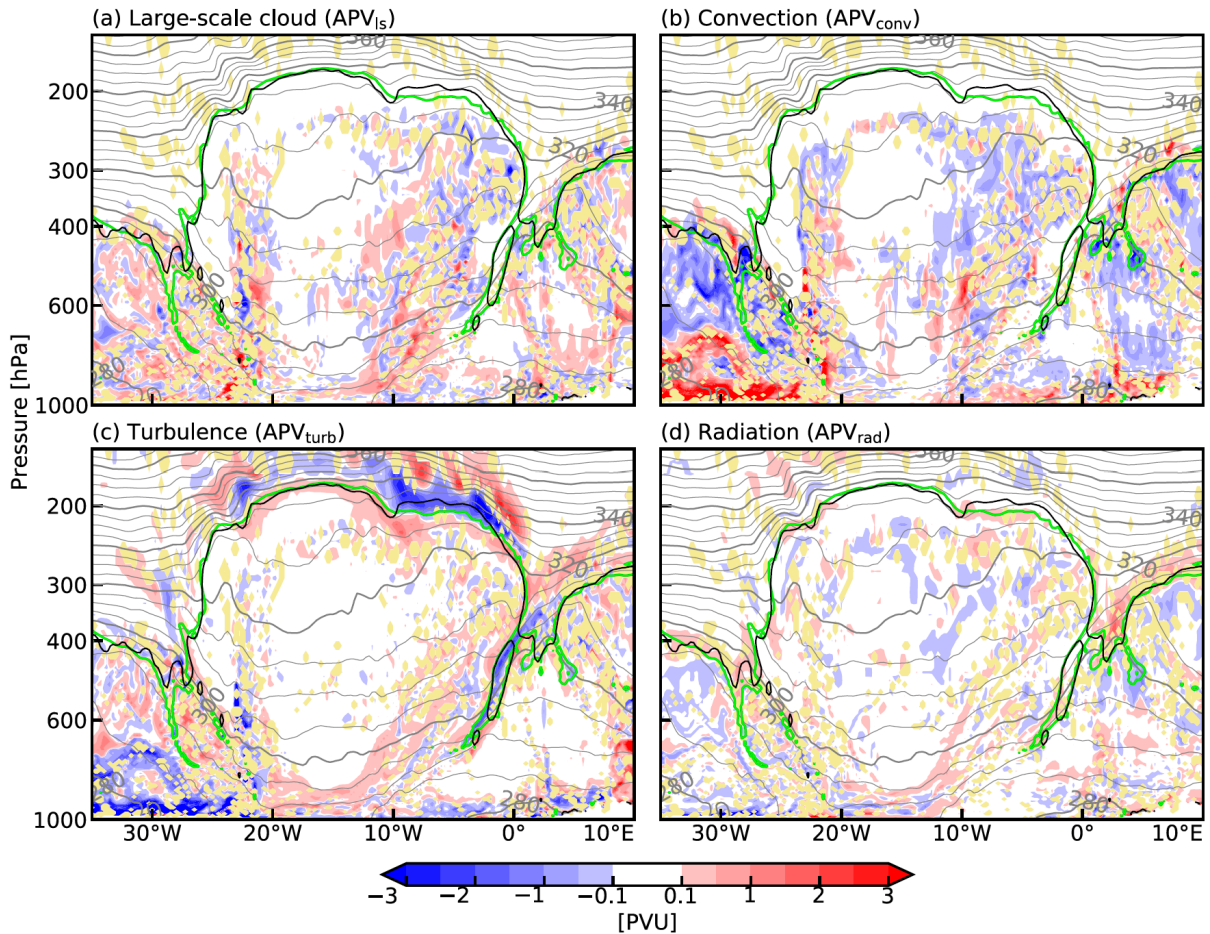


Figure 1.6: Vertical cross section at 48°N of 24 h accumulated PV at 00:00 UTC on 6 February 2017. Color shadings show accumulated PV contributions from individual processes, such as a) large-scale cloud scheme (APV_{ls}), b) convection scheme (APV_{conv}), c) turbulent processes (APV_{turb}), and d) radiation scheme (APV_{rad}). The solid black lines mark the 2 PVU contour of absolute PV, green lines mark the 2 PVU contour of advective PV. Gray lines denote isentropes. Figure taken from Spreitzer et al. (2019).

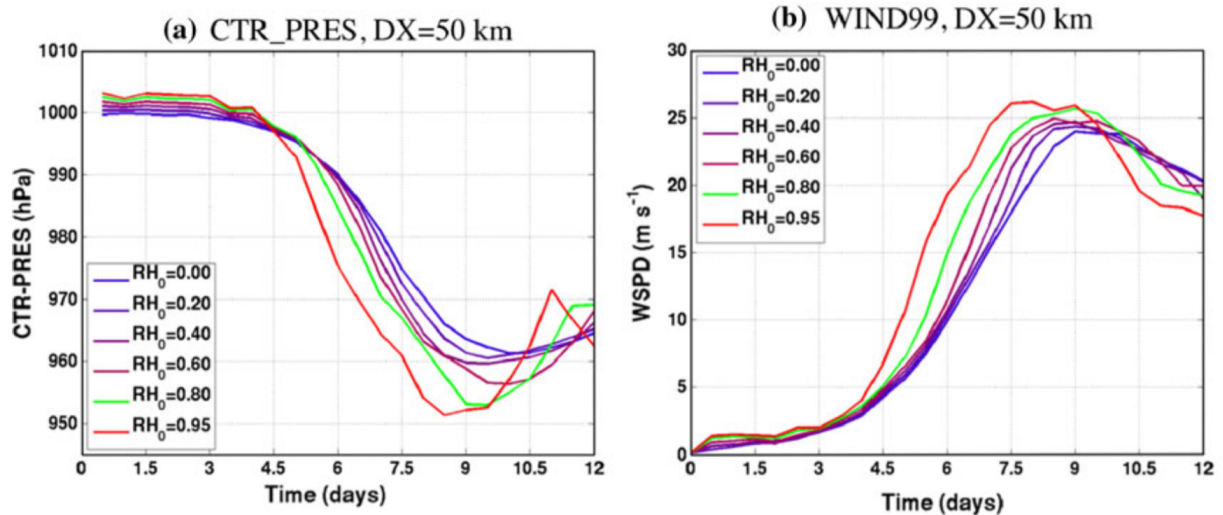


Figure 1.7: Results of idealized baroclinic life cycle simulations showing the impact of latent heating on ETCs by Booth et al. (2013b). The figure shows the temporal evolution of a) minimum surface pressure and b) surface wind speed for simulations with varying initial relative humidity (RH_0) values using a horizontal resolution of $dx = 50$ km. Blue lines mark the results with lowest RH_0 and red lines those with the highest RH_0 . Figure taken from Booth et al. (2013b).

In Figure 1.7, the impact of altering initial relative humidity, and thus latent heat release, on an idealized cyclone’s minimum surface pressure and surface winds are shown. The simulation with highest initial relative humidity ($RH_0 = 0.95$) creates the deepest cyclone, while setting initial relative humidity to 0 generates the weakest cyclone in terms of minimum surface pressure. Surface wind speed increases with higher moisture, as well as peak eddy kinetic energy (Booth et al., 2013b). Physically, this happens due to earlier saturation of rising air in the cyclone, which then leads to increased diabatic heating near the cyclone center. This is associated with a stronger low-level positive PV anomaly. This anomaly allows the cyclone to grow faster and get stronger (see Stoelinga, 1996).

Compared to latent heat release, radiation is a rather slow diabatic process and could arguably only have a subordinate effect on cyclones. However, Chagnon et al. (2013) found longwave radiation to be the prime process in producing positive diabatic modification of PV in upper-tropospheric levels of a North Atlantic cyclone. In their simulation, the vertical structure in radiative heating leads to positive diabatic PV above the troposphere and negative diabatic PV below, due to maximum longwave cooling at the tropopause.

Yet, the net of impact radiation on cyclone strength is not studied enough. Schäfer and Voigt (2018) were the first to show that radiation weakens the ETC’s strength by about 50% in terms of peak eddy kinetic energy and increases minimum surface pressure by 17 hPa. The weakening does not originate solely from the large-scale environment, but rather from radiative processes on a cyclone scale. Furthermore, they found that the radiation of clouds

plays an important role in the radiative weakening impact. These findings are described in more detail in section 1.3.

Due to the close connection between diabatic processes and temperature changes, the role of diabatic processes is located, energetically, in the eddy available potential energy, which modifies the eddy kinetic energy. The eddy and mean state energetics are described in the next section.

Lorenz Energy Cycle

The Lorenz energy cycle helps to explain the dynamics of ETCs. It describes the conversion from large-scale energy reservoirs to the small scale and vice versa.

Lorenz (1955) split the motion of the general atmospheric circulation not only into available potential energy (APE) and kinetic energy but also distinguished between the zonal and eddy available potential and kinetic energy. The zonal type acts as a sink or source for the eddy type and vice versa.

While kinetic energy in the atmosphere is the sum of the variances of the wind components, available potential energy consists of the variances of temperature. Zonal mean available potential energy (ZAPE) is thereby the variance of zonally averaged temperature. Eddy available potential energy (EAPE) marks the variance of temperature on a certain latitude circle. EAPE can be generated diabatically, linking diabatic processes directly to the Lorenz energy cycle (Haualand and Spengler, 2020).

Analogously to the temperature components, the variance of the zonally averaged wind velocity is called zonal mean kinetic energy (ZKE) and the wind velocity variance along a certain latitude is the eddy kinetic energy (EKE) (Lorenz, 1955). EKE therefore describes the "waviness" of the circulation.

Analytically, the four energy reservoirs, per unit area, can be described as followed (Lorenz, 1955):

$$\overline{\text{ZAPE}} = \frac{1}{2} \int_0^{\overline{p_0}} (\Gamma_d - \overline{\Gamma})^{-1} \overline{T}^{-1} \overline{[T]^2} dp \quad (1.1)$$

$$\overline{\text{EAPE}} = \frac{1}{2} \int_0^{\overline{p_0}} (\Gamma_d - \overline{\Gamma})^{-1} \overline{T}^{-1} \overline{T^{*2}} dp \quad (1.2)$$

$$\overline{\text{ZKE}} = \frac{1}{2} g^{-1} \int_0^{\overline{p_0}} \overline{[V]^2} dp \quad (1.3)$$

$$\overline{\text{EKE}} = \frac{1}{2} g^{-1} \int_0^{\overline{p_0}} \overline{V^{*2}} dp \quad (1.4)$$

where the square brackets denote the zonal mean of temperature T or wind velocity V and the overbar denotes the temporal mean. The asterisk marks the fluctuations of the zonal

mean, prime values are temporal fluctuations. p_0 is surface pressure and $\Gamma = -\partial T/\partial z$ the lapse rate of temperature, with Γ_d being the dry-adiabatic lapse rate. g is the acceleration of gravity.

ZAPE is a measure for baroclinicity, describing the tilt between temperature and pressure surfaces. EAPE shows the derivation from zonal mean temperature and is generated by cooling cold anomalies and warming warm anomalies. ZKE measures the jet stream strength and EKE gives the strength of the wind fields' eddies.

APE is generated when regions of low temperature are cooled or regions of high temperature are heated, due to the proportionality of APE generation to the covariance of diabatic heating and temperature. The gravity center of the atmosphere is raised and potential energy becomes available. Heat transport by eddies from tropical to polar regions decreases the mean temperature gradient between North and South and thus these eddies decrease ZAPE. Analogously, the poleward transport of angular momentum by eddies intensifies ZKE and is, therefore, a sink for EKE (Peixóto and Oort, 1984, p. 46f).

Since the Lorenz energy cycle describes transformations from large-scale to small-scale energy and vice versa, analyses of that cycle can help understanding how certain processes act. An example for such an analysis is shown in the following section.

1.3 Cloud-radiation interaction in extratropical cyclones

This section is based on Siebesma et al. (2020) and any other literature is referenced directly.

Most clouds in the extratropics are associated with ETCs, distributing clouds all along the major storm tracks. The cloud types vary from high-reaching clouds in uplift regions of ETCs to low, optically thick clouds near the cold fronts. Due to the close link between clouds and ETCs, the dynamic regimes in the midlatitudes can be estimated from cloud fields.

Clouds can influence the atmosphere via their radiative properties. Clouds can absorb and scatter shortwave radiation, and absorb and emit longwave radiation. This impact of clouds is described by the cloud-radiative effect (CRE), which is the difference between all-sky and clear-sky radiative flux

$$\text{CRE} = F_{\text{all-sky}}^{\text{net}} - F_{\text{clear-sky}}^{\text{net}} \quad (1.5)$$

where the net radiative flux F is the total rate of energy transported via radiation per area at a given level. It is often integrated over spectral intervals to have units of W m^{-2} and is defined by

$$F^{\text{net}} = F^{\downarrow} - F^{\uparrow} \quad (1.6)$$

The arrows denote if the radiative flux goes downward F^{\downarrow} , thus towards the surface, or

upward F^\uparrow , thus from the surface towards the top of the atmosphere (TOA). The equation for CRE holds for shortwave, longwave, and the sum of both.

If $F^{\text{net}} \neq 0$, energy is absorbed by layers ∂z of the atmosphere, turning into heating. The radiative heating rate in K day^{-1} is defined by

$$\frac{\partial T}{\partial t} = -\frac{1}{\rho c_p} \frac{\partial}{\partial z} F^{\text{net}} \quad (1.7)$$

where ρ is air density at a given level and c_p is the specific heat capacity at constant pressure.

Clouds contribute to the heating rate as well, and their contribution is described by cloud-radiative heating CRH, which is given by

$$\text{CRH} = -\frac{1}{\rho c_p} \frac{\partial}{\partial z} \text{CRE} \quad (1.8)$$

CRE is often computed at TOA or at surface levels. At TOA, clouds result in net cooling. Clouds hinder longwave radiation emitted by Earth to pass and, therefore, warm the system. The net effect at TOA is dominated by the reflection of shortwave radiation emitted by the sun from the clouds (Siebesma et al., 2020, p. 117). The overall CRE in the atmosphere is called atmospheric cloud-radiative effect (ACRE):

$$\text{ACRE} = \text{CRE}_{\text{TOA}} - \text{CRE}_{\text{SFC}} \quad (1.9)$$

with CRE_{TOA} and CRE_{SFC} being the sum of long- and shortwave CRE at TOA and the surface, respectively.

In the midlatitudes, CRE depend mainly on the the structure of ETCs. Optically thick clouds near the cold front prevent shortwave radiation to reach the surface, resulting in shortwave cooling of the surface and the atmosphere.

In deep-convective clouds, which are characteristic for uplift regions of ETCs, longwave radiative effects prevail shortwave radiative effects. The lower parts of deep-convective clouds absorb the outgoing longwave radiation from Earth. The upper parts of deep-convective clouds, on the other hand, reflect shortwave radiation back to the atmosphere and emit longwave radiation at lower temperatures, since longwave radiation is already absorbed in lower tropospheric levels. Thus, the cooling effect dominates, creating a radiative dipole in deep-convective clouds.

Cyclone strength and frequency can influence the radiative energy budget of the mid-latitudes. Tselioudis and Rossow (2006) found that increasing cyclone strength results in increased shortwave cooling and longwave warming due to higher reaching and optically thicker clouds. In total, a 5% increase in storm strength leads to 1.5 W m^{-2} net cooling. If the frequency of ETCs decreases, the amount of clouds decreases too - leading to net warming of the atmosphere.

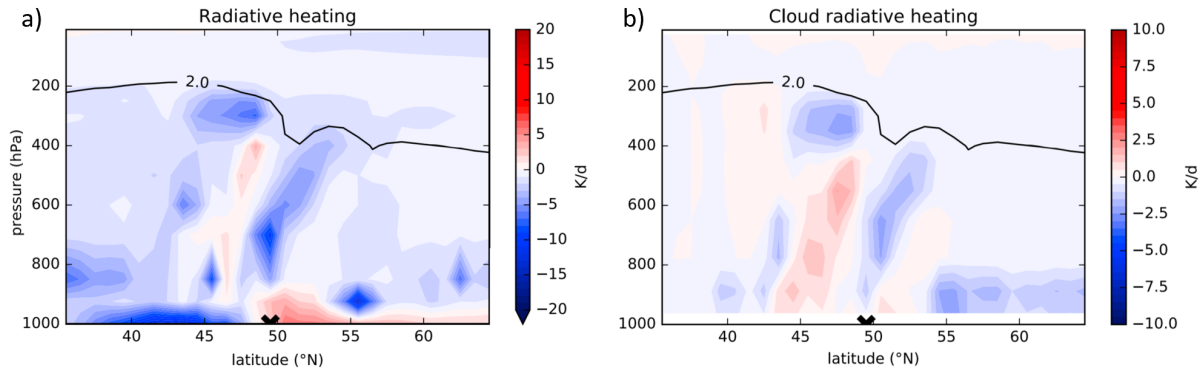


Figure 1.8: Vertical cross section through the cyclone center, showing a) radiative heating and b) cloud radiative heating in K/d. The location of minimum surface pressure is marked by the black "v". Figure taken from Schäfer and Voigt (2018), adapted.

It has not only been found that ETCs influence clouds, but also the other way around, via their radiative effects. ACRE was found to dampen storm track intensity at lower tropospheric levels (Grise et al., 2019) and to change the eddy-driven jet (Watt-Meyer and Frierson, 2017). Li et al. (2015) showed that ACRE increases EKE by up to 30% near the midlatitude tropopause and decreases static stability just below the the tropopause.

Furthermore, Schäfer and Voigt (2018) provided evidence that ACRE weakens idealized ETCs. By comparing simulations where the radiation scheme was enabled (“all-sky radiation”), partly enabled (“clear-sky radiation”) or disabled (“no radiation”), they found that radiative heating weakens the ETC, with peak EKE being reduced by 50%. Cloud radiation is accountable for 30% to 50% of this weakening.

Schäfer and Voigt (2018) inspected the contribution of CRH to the vertical structure of radiative heating in the cyclone. Radiative heating around the cyclone center shows a vertical dipole where radiation heats the lower troposphere and cools the upper troposphere (Figure 1.8a). This dipole is mostly caused by cloud radiation (Figure 1.8b) and is characteristic for cloud radiation of deep-convective clouds in a vertical profile .

In their simulations with all-sky and clear-sky radiation, Schäfer and Voigt (2018) found substantial large-scale radiative cooling within the simulated first 3 days, marked by a strong temperature decrease in the atmosphere (Figure 1.9, clear-sky not shown). The radiative cooling is partly compensated by latent heating in the southerly region of the domain, but overall, the atmosphere remains being strongly cooled. In contrast, the simulation without radiation shows very little initial adjustment in terms of temperature changes and accumulated latent heating by day 3 (Figure 1.9a and d).

As this radiative cooling might contribute to changes in cyclone strength, Schäfer and Voigt (2018) analyzed the Lorenz energy reservoirs of the system. However, they found that radiative impacts arise on cyclone-scale, not on global scales. This is depicted in Figure 1.10, where zonal mean moist available potential energy (MAPE) declines due to conversion into

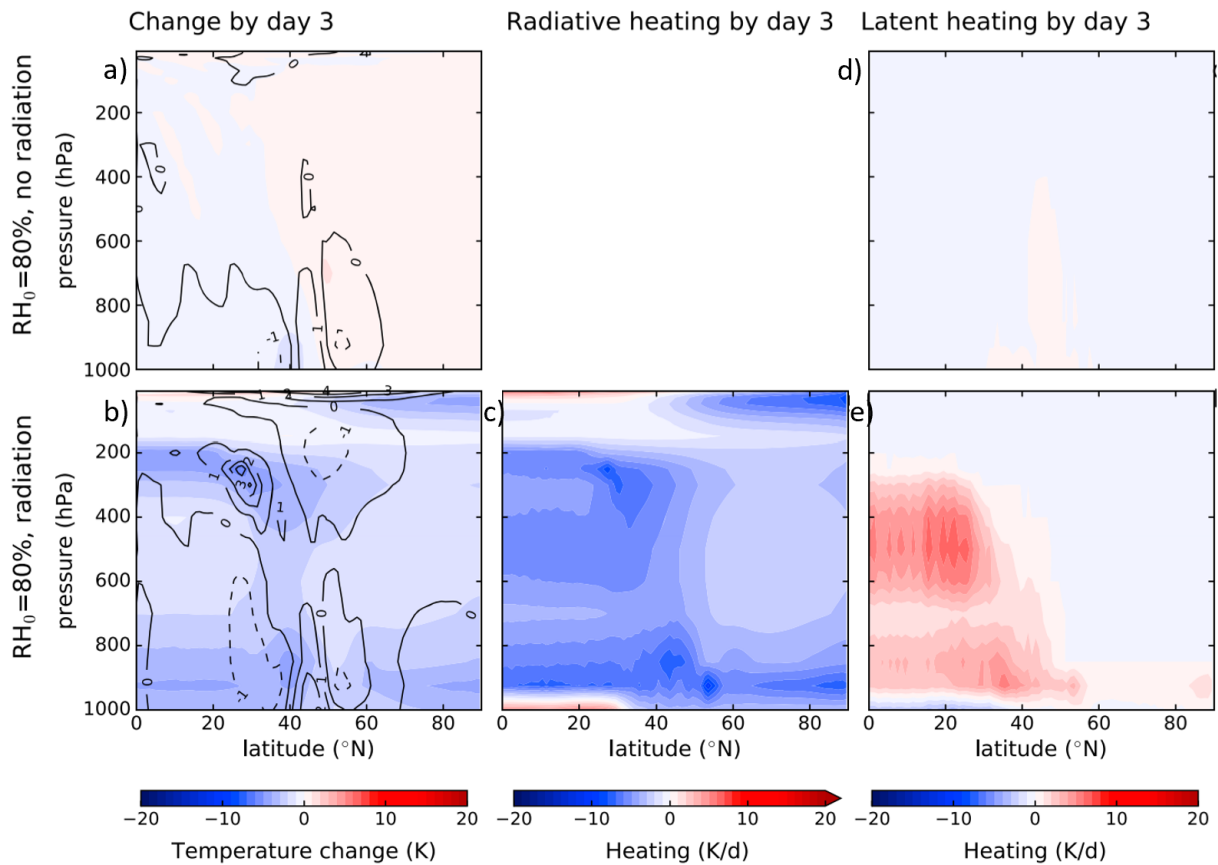


Figure 1.9: Zonal mean of changes in temperature (color shadings) and zonal wind speed (in m/s, contours) by day 3 in the simulation a) without radiation and b) with all-sky radiation. c) Accumulated radiative heating by day 3 in K/d. d, e) Accumulated latent heating by day 3 in the simulation without radiation and with all-sky radiation, respectively. Figure taken from Schäfer and Voigt (2018), adapted.

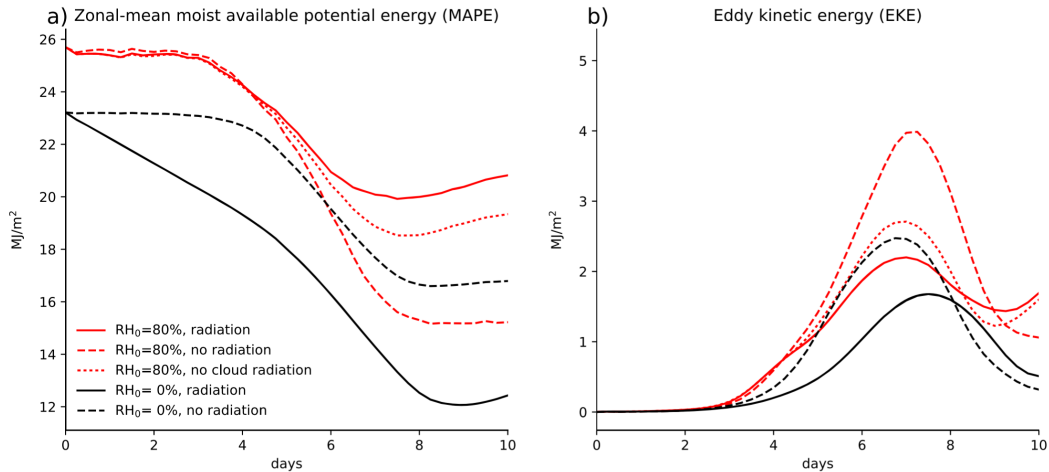


Figure 1.10: Vertically integrated Lorenz energy reservoirs for simulations with all-sky radiation, clear-sky radiation and no radiation settings. a) Zonal mean moist available potential energy, b) eddy kinetic energy, both in MJ/m². Simulations with initial humidity of 80% are marked in red. Initially dry simulations with $RH_0 = 0\%$ are marked in black. Figure taken from Schäfer and Voigt (2018).

EKE. In contrast to ZAPE (see section 1.2), MAPE holds the impacts of moisture and latent heating. As the radiation settings only have an impact on MAPE as soon as the cyclone is already developing, Schäfer and Voigt (2018) concluded that the radiative impact does not originate in the large-scale potential energy reservoir.

Moreover, the radiative impact is comparable in magnitude to the impact of latent heat release on an ETC, albeit latent heating rates are considerably stronger than radiative heating rates. Latent heating is only active during cloud formation, while cloud-radiative heating acts throughout the whole life span of a cloud. Schäfer and Voigt (2018) hypothesized that due to these temporal differences, radiative heating impacts can maintain the same impact magnitude as latent heating.

2 | Research questions

The results of Schäfer and Voigt (2018) call for a more systematic study of the role of CRH. The mechanisms behind radiation-induced cyclone weakening were hypothesized, but not confirmed. The initial radiative cooling in all-sky and clear-sky simulations does not resemble the reference simulation, which is the simulation without radiation. Using an improved simulation setup, I want to test the results by Schäfer and Voigt (2018) and focus on CRH impacts.

In order to investigate how ETCs are affected by CRH, I will address the following questions:

1. **To what extent are the results from Schäfer and Voigt (2018) robust?**

Schäfer and Voigt (2018) only used one model version. As model physics develops, I want to see if their results are robust using two updated model versions. This allows a rather insightful comparison of CRH impacts and grants to make statements about the robustness of the conclusions from Schäfer and Voigt (2018).

Furthermore, the initial adjustment in their all-sky and clear-sky simulations is fixed by using new simulations that preserve the large-scale background state similar to the reference simulation. This allows me to make clearer statements and more direct comparisons between simulations with cloud radiation and without radiation.

2. **Is there an altitude dependency of cloud-radiative heating?**

Schäfer and Voigt (2018) compared all-sky and clear-sky radiative heating impacts and concluded the overall radiative heating impact from clouds. With new simulation sets, I investigate the impact of clouds in more detail and study how CRH at different height levels affects ETCs.

3 | Methods

In this chapter, I document the methodological setup of my idealized baroclinic life cycle simulations. I will start by explaining the idea behind baroclinic life cycles and then describe the initial conditions and the model setup. Furthermore, I will explain the simulations, the method to isolate the impact of cloud-radiative heating, and my analysis strategy.

3.1 Baroclinic life cycles

Idealized baroclinic life cycles have the advantage of highly controlled settings, which can be used to study the dynamics of ETCs. They allow one to focus on a certain effect or to isolate a process by disabling other factors. Many studies used baroclinic life cycles, e.g., to examine transport of chemical air masses (Polvani and Esler, 2007), diabatic processes (e.g. Schäfer and Voigt, 2018; Boutle et al., 2011), or radiative impacts of CO₂ (Kaviani et al., 2022).

Thorncroft et al. (1993) described two types of baroclinic life cycles, life cycle type 1 (LC1) and type 2 (LC2). The two setups differ in the background of the initial conditions, resulting in different evolution of the cyclones. LC1 features early cyclonic evolution, changing to primarily anticyclonic circulation in the mature stages of the life cycle (Figure 3.1, shown by PV on the 335 K isentropic surface). The cold front is well-developed and the anticyclonic tongue breaks equatorward of the system. LC2 develops into a very pronounced cyclonic circulation with strong warm fronts and a longer, stronger intensification phase (Figure 3.1, LC2). In the cyclonic part of the life cycle, warm air gets trapped in the low-pressure center.

The wind distribution of the initial conditions of LC1 has its zonal maximum approximately at 45°N latitude, without any surface winds (Figure 3.2). LC2, on the other hand, has an additional barotropic contribution of westerlies southward and easterlies northward of the wind maximum in LC1, and, therefore, also increased cyclonic shear of the zonal-mean wind. A temperature perturbation is initially introduced into the zonal mean flow. The initial conditions for LC1 are described in detail in section 3.1 since I use only LC1 for the simulations.

Dynamically, a baroclinic life cycle simulation uses nearly inviscid, dry, adiabatic primitive equations on a sphere (Polvani and Esler, 2007):

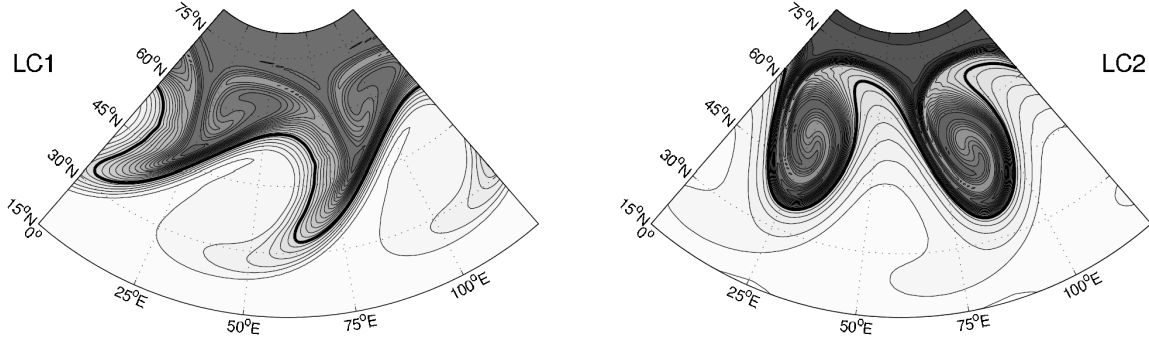


Figure 3.1: Ertel potential vorticity at day 7 (LC1, left) and day 8 (LC2, right) on the 335 K isentropic surface. The 2 PVU contour is in bold, the other contours are in 0.25 PVU intervals. LC1 is the life cycle type use in my simulations. Figure from Polvani and Esler (2007).

$$\frac{d\mathbf{u}}{dt} + f\mathbf{k} \times \mathbf{u} + \nabla_h \Phi + \frac{RT}{p_s} = \nu \nabla_h^6 \mathbf{u} \quad (3.1)$$

$$\frac{dT}{dt} - \frac{\kappa T}{\sigma p_s} \omega = \nu \nabla_h^6 T \quad (3.2)$$

$$\frac{\partial p_s}{\partial t} + \int_{\sigma_T}^1 \nabla_h \cdot (p_s \mathbf{u}) d\sigma = 0 \quad (3.3)$$

in σ coordinates for horizontal velocity \mathbf{u} , temperature T and surface pressure p_s . The Coriolis parameter is $f = 2\Omega \sin \varphi$, ∇_h is the horizontal gradient operator. σ is defined by p/p_s with p being the pressure of the fluid. R denotes the ideal gas constant, κ the heat capacity ratio, Φ the geopotential and ω the pressure vertical velocity. σ_T marks the model top, the model surface is flat ($\sigma = 1$). ν in the hyperdiffusion terms on the right hand side in equation 3.1 and 3.2 is dependent of the horizontal resolution.

In this thesis, I use the same setup as in Schäfer and Voigt (2018) and thus focus on LC1 simulations. The model setup is described in detail in section 3.2.

The initial conditions for LC1 simulations are exactly as in Schäfer and Voigt (2018). Most of their initial conditions follow Polvani and Esler (2007). The initial zonal wind is defined by

$$u_1(\varphi, z) = U_0 F(\varphi) \left[(z/z_T) e^{-[(z/z_T)^2 - 1]/2} \right] \quad (3.4)$$

The wind velocity U_0 has its maximum at z_T , the log-pressure height $z \equiv H \log p_0/p$ acts as a proxy for pressure p and the latitudinal dependence $F(\varphi)$ is defined as

$$F(\varphi) = \begin{cases} [\sin \pi (\sin \varphi)^2]^3 & \text{for } \varphi > 0 \\ 0 & \text{for } \varphi < 0 \end{cases} \quad (3.5)$$

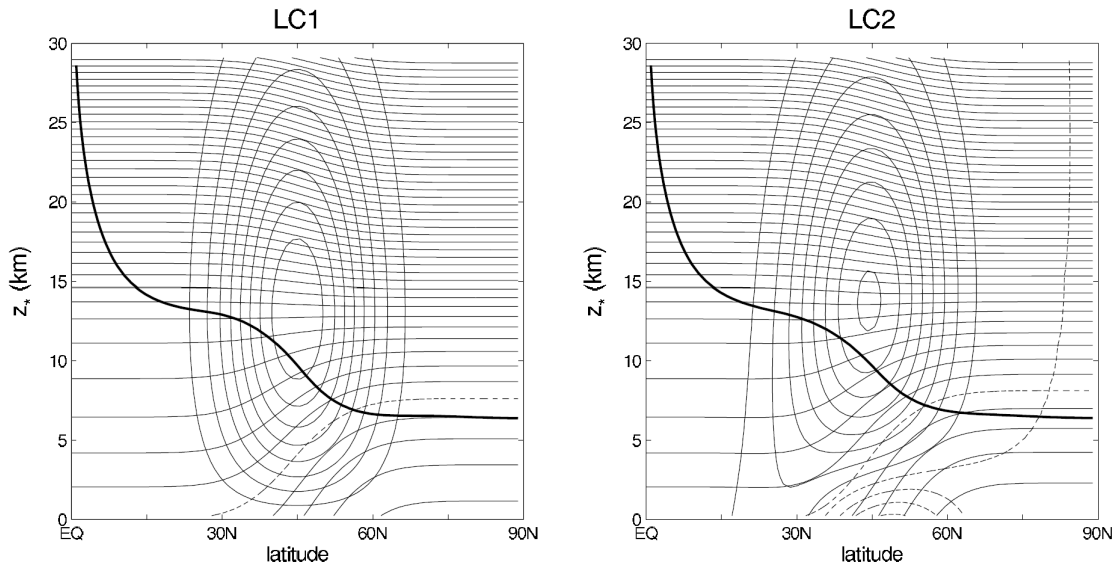


Figure 3.2: Initial winds and potential temperature for LC1 (left) and LC2 (right). Potential temperature is shown in 10 K contour intervals. The 300 K isentrope is shown by the dashed line. Winds have contour intervals of 5 m s^{-1} , where negative contours are dashed. The position of the 2 PVU surface is marked by the bold line. Figure taken from Polvani and Esler (2007).

with a maximum at $\varphi = 45^\circ\text{N}$. The baroclinically unstable wind is initially in thermal wind balance with the zonally uniform temperature field, just as the one shown in Figure 3.2 for LC1. There are no initial vertical or meridional winds and the setup starts without initial clouds or precipitation. To trigger cyclones, a sine-shaped temperature perturbation is added:

$$T'(\lambda, \varphi) = \hat{T} \cos m\lambda [\text{sech}(m(\varphi - \hat{\varphi}))]^2 \quad (3.6)$$

T' denotes the temperature perturbation dependent of longitude λ and latitude φ . $m = 6$ is the wave number. The wave amplitude \hat{T} is set to 1 K. The perturbation develops along 45°N (see Figure 3.3). With this perturbed and baroclinically unstable field, six similar cyclones are generated.

The initial relative humidity is defined by

$$\text{RH} = \begin{cases} \text{RH}_0 \cdot (1 - 0.85 \cdot z/z_T)^{5/4} & \text{for } z < 14 \text{ km} \\ 0 & \text{for } z > 14 \text{ km} \end{cases} \quad (3.7)$$

where $\text{RH}_0 = 80\%$ to simulate wintertime storm track climatologies and the scale height is set to $z_T = 12 \text{ km}$. In order to ensure that SST cannot respond to the cyclone evolution, SST are fixed to temperatures 0.5 K lower than the unperturbed temperatures of the lowest model layer during initialization. Thus, the surface radiates thermally and can reflect shortwave radiation, but the impact of atmospheric radiative heating is isolated because SST cannot respond to the cyclone.

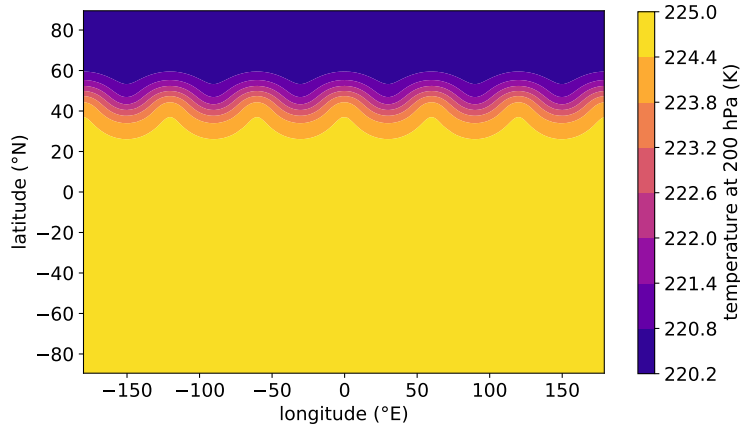


Figure 3.3: The initial temperature perturbation is a sine-shaped wavenumber 6 perturbation, shown at 200 hPa in K.

The synoptic evolution of a simulated cyclone with ICON 2.6 is shown in Figure 3.4, using the simulation without radiation. On day 3, early stages of cloud and precipitation development are visible. PV starts to amplify. On day 5, cloud and precipitation fields are already more pronounced, just as high- and low-pressure areas. The 2 PVU wave is shifting equatorward of the system. On day 7, the precipitation field marks the frontal area, and clouds dominate the domain. The 2 PVU wave shows anticyclonic wave breaking, which is characteristic of LC1 and similar to the PV pattern shown in Figure 3.1.

3.2 ICON model and model setup

Following the setup from Schäfer and Voigt (2018), I use the ICON model (ICOsahedral Non-hydrostatic atmosphere model) in its NWP (numerical weather prediction) configuration. This model is a joint project by Deutscher Wetterdienst, Max Planck Institute for Meteorology, Karlsruhe Institute of Technology, and Deutsches Klimarechenzentrum. Its advantages lie in the unified approach of using the same model for NWP and climate modeling (Zängl et al., 2015; Prill et al., 2019). I use several versions for the simulations, precisely the ICON-NWP versions 2.015, 2.1.00, and 2.6.2.2. Throughout the thesis, I will address these model versions by ICON 2.0, ICON 2.1, and ICON 2.6, respectively. All model runs with ICON 2.1 and ICON 2.6 are performed by myself on Mistral (HLRE-3, High Performance Computing system for Earth system research), which was the first petascale supercomputer of Deutsches Klimarechenzentrum (DKRZ). All ICON 2.0 output has been computed by Sophia Schäfer and Aiko Voigt on the IC2 and ForHLR2 supercomputers (Schäfer and Voigt, 2018).

My model setup is the same as the one used in Schäfer and Voigt (2018). Each simulation is run for 14 days with the model output written every six hours. The model time step of the dynamical core is set to $\Delta t = 180$ s with 90 vertical levels at an R2B6 horizontal resolution, corresponding to approximately 40 km. Schäfer and Voigt (2018) found their results to

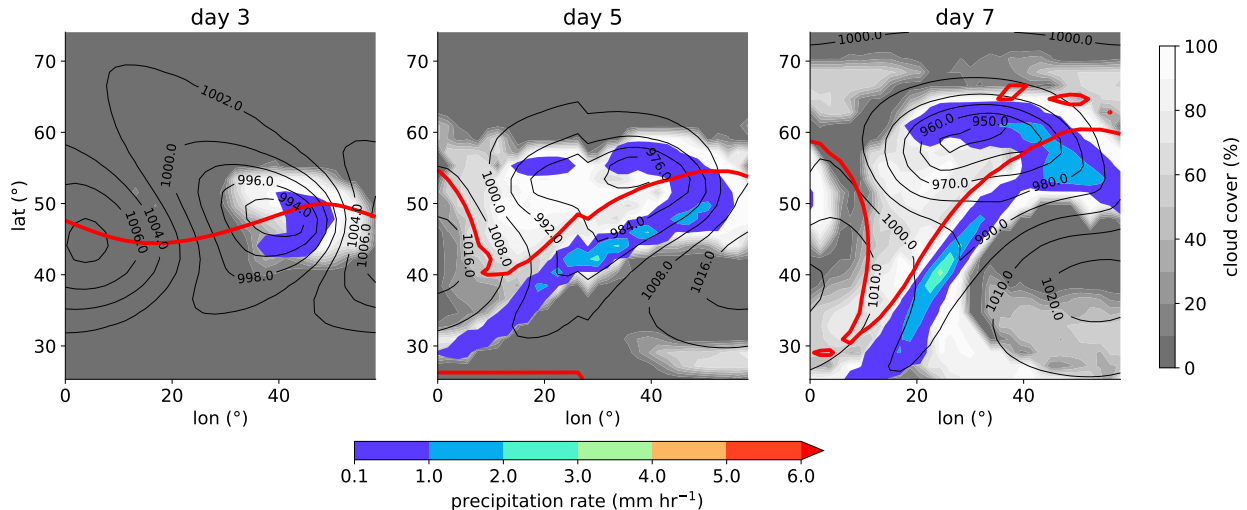


Figure 3.4: Evolution of pressure (contours), precipitation (colors) and cloud cover (gray shadings) at day 3, 5 and 7 for the baroclinic life cycle simulation without radiation using ICON 2.6. The red contour marks the dynamical tropopause at the 300 hPa pressure level defined as the 2 PVU contour. Please note the different pressure contour intervals.

be insensitive to resolution. The horizontal resolution of the model output is set to $1^\circ \times 1^\circ$ for ICON 2.1 and $1.875^\circ \times 1.875^\circ$ for ICON 2.6, although I also have ICON 2.6 output at a $1^\circ \times 1^\circ$ grid, but with a higher model time step ($\Delta t = 320$). Analyses showed the horizontal resolution of the model output had no significant impacts on the final results.

I use the single-moment scheme described by Doms et al. (2011) for cloud microphysics, the prognostic TKE scheme by Bechtold et al. (2008) for turbulent transfer, and the diagnostic PDF scheme for cloud cover by M. Köhler et al. (DWD) (Prill et al., 2019). For radiation, I apply the Rapid Radiative Transfer Model (RRTM, Mlawer et al., 1997). All other processes are configured according to Prill et al. (2019).

Aerosol-radiative interactions are neglected, ozone and all atmospheric radiative characteristics are set to the same values as in Williamson et al. (2012), which are widely used in aquaplanet setups. Greenhouse gases are set to approximate present-day values ($\text{CH}_4 = 1650$ ppbv, $\text{N}_2\text{O} = 396$ ppbv, $\text{CO}_2 = 348$ ppmv, no CFCs). Insolation is set to equinox conditions with a diurnal cycle.

One of the main changes between the model versions 2.1 and 2.6 that might be important for my work is the fix of a bug within the physics-dynamics coupling of the turbulence scheme, the so-called “ c_p/c_v bug”. The turbulence scheme was originally developed for coupling the physics and dynamics at constant pressure, while ICON uses coupling at constant density. However, in ICON 2.0 and 2.1, the factor $c_p/c_v = 1.4$ is missing in the conversion of the turbulent heat flux divergence, affecting the energy balance of the model (Zängl and Schäfer, 2021). The turbulence scheme in ICON 2.0 and 2.1, therefore, creates larger surface fluxes than in ICON 2.6. This leads to different clouds in the two model versions, consistent with

the bug.

3.3 Simulations

In order to isolate the effect of CRH, I use various simulation strategies. Depending on the simulation, radiation is either fully passed to the dynamical core, passed partly or not at all. This is shown by the thermodynamic equation where the term RAD marks the contribution of radiative heating rates:

$$c_p \frac{dT}{dt} - p \frac{d\alpha}{dt} = RAD + J \quad (3.8)$$

This equation is equivalent to equation 3.2, but including diabatic effects. The nomenclature is now different in order to use the right hand side of the equation for alterations in radiation. On the left hand side, the first term of the equation consists of the specific heat capacity at constant pressure c_p and the temporal derivative of temperature T . The second term marks work by pressure and consists of pressure p and the temporal derivative of specific volume α . On the right hand side, J holds hyperdiffusion and all heating rates due to diabatic processes except radiation. RAD contains radiation from the whole atmosphere and will be called all-sky radiation throughout the thesis. When clouds are set transparent, the remaining radiation is called clear-sky radiation RAD_{clear} .

To isolate CRH, RAD_{clear} is subtracted from RAD_{all} . The thermodynamic equation now changes to

$$c_p \frac{dT}{dt} - p \frac{d\alpha}{dt} = \underbrace{(RAD_{all} - RAD_{clear})}_{RAD_{cloud}} + J \quad (3.9)$$

In this case, the model computes $RAD_{all} - RAD_{clear} = RAD_{cloud}$ and passes the result to the dynamical core instead of RAD_{all} . This solves a problem that was already addressed in Schäfer and Voigt (2018) concerning the initial evolution of radiative cooling (see section 1.3). The simulations with all-sky and clear-sky radiation develop strong radiative cooling in the atmospheric background within the first 3 days (Figure 3.5a, b), especially in the southern areas of my analysis domain. Therefore, the large-scale environment at the beginning of cyclone development at day 3 is substantially cooler than in the simulation without radiation (Figure 3.5c) and radiation could impact the cyclone via large-scale influences, leading to sooner saturation of rising air and thus, early precipitation.

However, changes from day 0 to day 3 in the simulation with only cloud radiation remain rather small (Figure 3.5d), similar to the development simulation without radiation. The radiative cooling arises only from clear-sky radiation, which is disabled in the simulation with only cloud radiation. To address the impact of CRH on ETCs, the large-scale initial background should evolve the same as in the reference simulation, which is the simulation

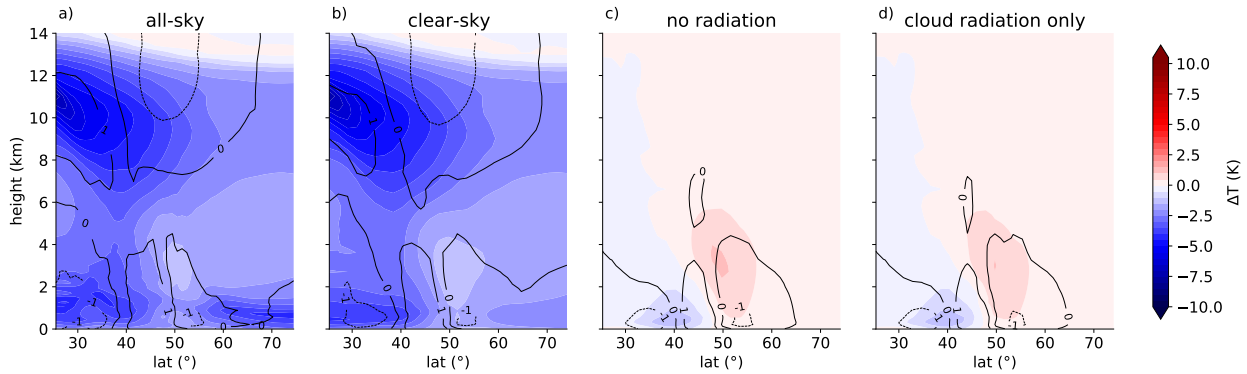


Figure 3.5: Changes of zonal mean temperature in K and zonal mean wind in m s^{-1} by day 3 for simulations with a) all-sky radiation, b) clear-sky radiation, c) no radiation and d) cloud radiation only, using ICON 2.6. Changes of zonal mean temperature are depicted by color shadings, zonal mean wind changes by contours.

without radiation. Therefore, the new simulation where ETCs are heated with only cloud radiation is more suitable and I will discuss these simulations most extensively throughout the thesis. The initial adjustment in ICON 2.1 is not shown as it is similar to the initial adjustment in ICON 2.6.

Additionally, the simulation with cloud radiation can be altered to only use cloud radiation in certain height levels, e.g. cloud radiation in the boundary layer or only cloud radiation in free tropospheric levels. To focus on cloud-radiative heating in the boundary layer, the model code is modified to set all shortwave and longwave heating rates either above a certain altitude, e.g. 2 km, to 0. For only free tropospheric CRH, all heating rates below the given altitude are set to 0. The dynamical core then uses these updated heating rates. The vertical profiles of domain mean CRH rates at day 6 are shown in Figure 3.6. For demonstration purposes, one value outside of the figure range in the simulation with only CRH and in the simulation with only CRH in the boundary layer is not depicted. In both simulations, this one value is smaller than -4 K day^{-1} .

In total, I use six different simulation setups, which are listed in Table 3.1.

3.4 Analysis methods

The baroclinic life cycle simulation creates 6 similar cyclones on the Northern Hemisphere. For analysis, I consider the area in which cyclones develop - 25°N to 75°N - as the domain. The considered data d is area-weighted and averaged over the domain to get the domain mean \bar{d} :

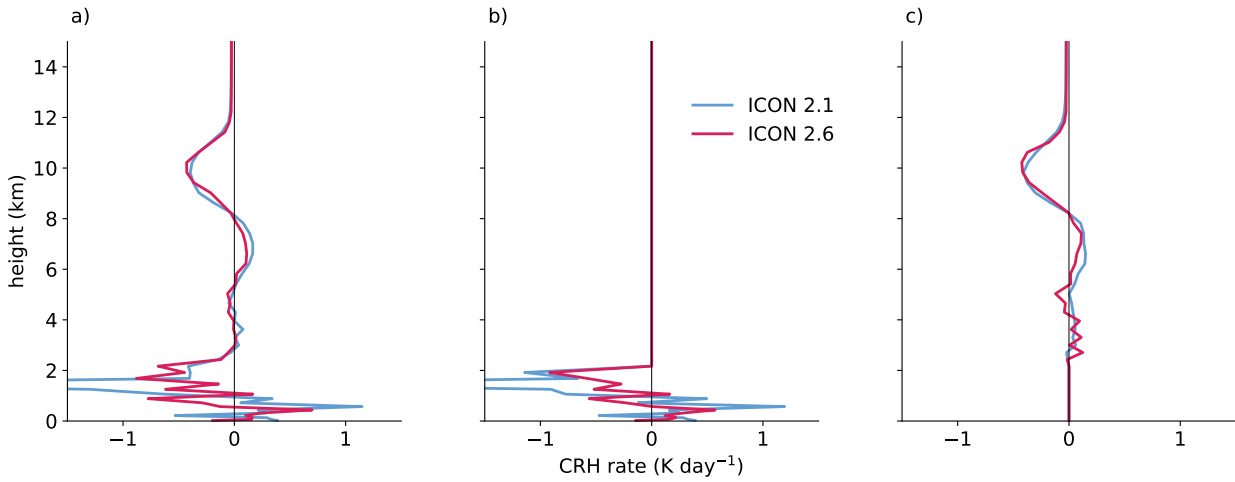


Figure 3.6: Vertical profile of domain mean cloud-radiative heating rates in K day^{-1} at day 6 for simulations with a) cloud radiation, b) cloud radiation below 2 km and c) cloud radiation above 2 km.

Table 3.1: Description of the simulation setups, including the abbreviations by which I will address them throughout the thesis.

Abbr.	Simulation name	Description	New simulation
R_0	No radiation	Radiation scheme is turned off. Reference simulation.	
R	All-sky	Radiation fully interacts with the cyclone.	
C_0	Clear-sky	Clouds are transparent, only clear-sky radiative fluxes are used.	
C	CRH only	Only cloud radiation interacts with the cyclone.	x
C_{BL}	Boundary layer CRH only	Only CRH below 2 km is passed to the dynamical core, CRH above 2 km is set to 0.	x
C_{FT}	Free-tropospheric CRH only	Only CRH above 2 km is passed to the dynamical core, CRH below 2 km is set to 0.	x

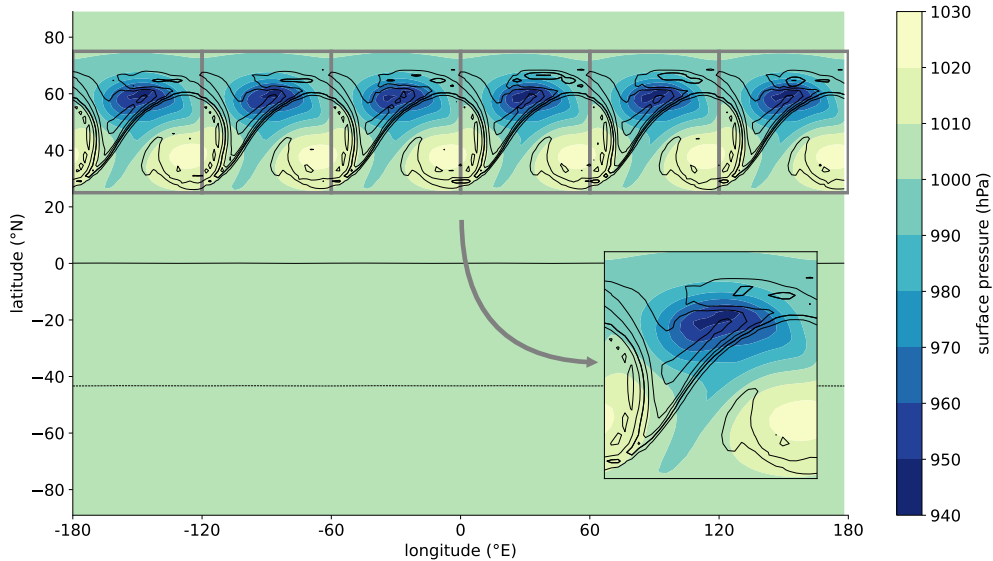


Figure 3.7: Demonstration of mean cyclone analysis. The colors show surface pressure in hPa, the black contours show PV at the 300 hPa level on day 7. The 2 PVU contour marking the dynamical tropopause is bold, the other contours are in 1 PVU intervals. The gray frames mark the six chunks the domain is parted into. The larger depicted cyclone in the lower right is the resulting mean cyclone.

$$\bar{d} = \frac{\int_{\lambda=-180^{\circ}}^{180^{\circ}} \int_{\varphi=25^{\circ}}^{75^{\circ}} d_{\lambda,\varphi} \cos \frac{\varphi\pi}{180^{\circ}} d\lambda d\varphi}{\int_{\varphi=25^{\circ}}^{75^{\circ}} \cos \frac{\varphi\pi}{180^{\circ}} d\varphi} \quad (3.10)$$

I am interested in the CRH of a single cyclone, therefore I average over the 6 produced cyclones. I construct this mean cyclone by chunking the data into smaller parts of 60° longitude λ length along the latitude φ domain at a given time t_c . The resulting 6 chunks c are then summed up and divided by the number of cyclones:

$$\bar{c} = \frac{1}{6} \sum_{i=1}^6 c_i \quad (3.11)$$

The resulting mean cyclone is depicted in Figure 3.7, which shows surface pressure and upper-level PV contours on day 7. The gray rectangles mark the chunks which are then averaged to the cyclone at which the arrow is pointing. The domain is given by the area of the rectangles.

EKE is used as the prime metric for cyclone strength, which is an energy reservoir in the Lorenz energy cycle (see Section 1.2). At a given pressure level p , EKE is given by

$$\text{EKE}|_p = \frac{(u'^2 + v'^2)_p}{2} \quad (3.12)$$

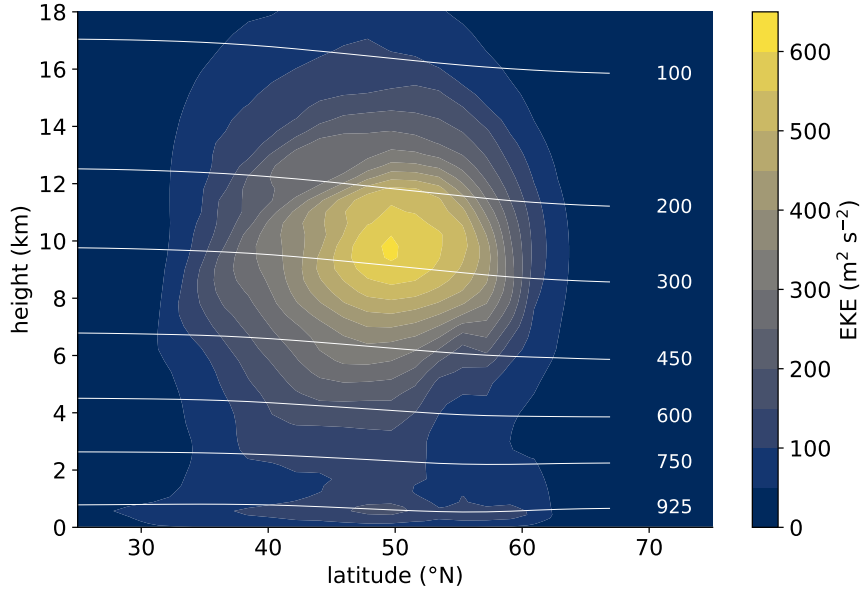


Figure 3.8: Zonal mean EKE in m^2s^{-2} at day 6 in simulation R_0 with ICON 2.6, shown by color shadings. The white contours show the pressure levels in hPa.

where

$$u'(t, \lambda, \varphi) = u(t, \lambda, \varphi) - \bar{u}(t, \varphi) \quad (3.13)$$

$$v'(t, \lambda, \varphi) = v(t, \lambda, \varphi) - \bar{v}(t, \varphi) \quad (3.14)$$

are the horizontal wind eddy components dependent of time t , longitude λ and latitude φ . Vertical wind components are neglected. When mentioning EKE in this thesis, it is given as the domain mean described above unless stated otherwise. The zonal mean EKE at day 6 of simulation R_0 in ICON 2.6 is shown in Figure 3.8. I will analyze EKE predominantly at the 300 hPa level, where EKE has approximately its maximum, and at the 925 hPa level, showing lower tropospheric EKE development.

The model outputs the data on 90 vertical height levels. However, I use pressure levels for my EKE analyses, for which I interpolate the data to pressure levels during postprocessing.

Additionally, I analyze the minimum surface pressure. To do so, the pressure of the mean cyclone is computed, of which I then take the minimum value. However, minimum surface pressure is a point metric, therefore EKE is a better metric for cyclone strength as it captures the large scale evolution.

I can isolate CRH impact on a quantity by subtracting the result of one simulation from another. Schäfer and Voigt (2018) did this by subtracting clear-sky simulation results from all-sky results. The new simulations extend the range of CRH impact calculations, allowing me to make statements about the robustness of the results:

$$\text{CRH impact} \simeq C - R_0 \quad (3.15)$$

$$\simeq (C - C_{FT}) + (C - C_{BL}) \simeq 2C - C_{BL} - C_{FT} \quad (3.16)$$

$$\simeq (C_{BL} - R_0) + (C_{FT} - R_0) \simeq C_{FT} + C_{BL} - 2R_0 \quad (3.17)$$

$$\simeq R - C_0 \quad (3.18)$$

Equation 3.15 is the difference between the simulation with only cloud radiation C and the simulation without radiation R_0 , which, obviously, marks the CRH impact. This is the most straightforward approach.

In Equation 3.16, I add the CRH impacts of boundary layer clouds and clouds within the free troposphere. In this case, the CRH impact of boundary layer cloud radiation is represented by the first term in brackets, thus the difference between the examined quantity of the simulation with only cloud radiation C and that of the simulation with only CRH from the free troposphere C_{FT} . Analogously, the CRH impact of clouds in the free troposphere is given by the difference between simulation C and the simulation with boundary layer CRH, C_{BL} , which is the second term in brackets.

Analogously, the isolated CRH impacts of boundary layer clouds and clouds within the free troposphere can be also computed by subtracting the simulation without radiation R_0 from C_{BL} or C_{FT} (Equation 3.17). The sum of these terms is then again the overall CRH impact.

As a reference, I added Equation 3.18 to show the approach by Schäfer and Voigt (2018). The CRH impact is here defined as the difference between the all-sky simulation R and the clear-sky simulation C_0 .

I will use this approach mostly when making statements about peak EKE, but it is not limited to that.

4 | Results

In this chapter I present the results of my work, starting with a comparison with the results of Schäfer and Voigt (2018) and then moving on to the results of my cloud radiation simulations. Moreover, I will discuss the findings on how clouds at certain levels affect the cyclone strength.

4.1 Reproducing the results of Schäfer and Voigt (2018) with ICON 2.1

The very first step is to reproduce the results of Schäfer and Voigt (2018), who used ICON 2.0, with ICON 2.1 to see the robustness of radiative impact on cyclone strength. The question of robustness raises due to the change of the model version and of the High Performance Computing system. Furthermore, I am then not limited on the outputs by Schäfer and Voigt (2018) and can use my own simulations for detailed analysis.

The comparison of EKE shows no significant differences (Figure 4.1). Throughout 10 days of the cyclone's life span, ICON 2.0 and 2.1 simulations show similar evolution. Cyclone development starts around day 3. The simulated cyclones reach peak strength around day 7, reaching EKE values at 300 hPa near $100 \text{ m}^2\text{s}^{-2}$ in the simulations without radiation (Figure 4.1a). Peak EKE is reduced by approximately 50% when radiation is switched on. The cyclone's peak EKE at 300 hPa is 15.7% lower in the all-sky than in the clear-sky simulation.

At lower tropospheric levels (Figure 4.1b), the weakening effects can also be observed. The simulation without radiation shows the strongest cyclone in terms of EKE. Clear-sky radiation weakens it, and turning on radiation fully leads to the weakest cyclone development. In the all-sky simulation, EKE peaks twice in lower tropospheric levels, once on day 5 and then again on day 7.

In terms of minimum surface pressure, ICON 2.0 and ICON 2.1 produce very similar values as well (Figure 4.2). The simulation without radiation shows the lowest minimum surface pressure, which is reached around day 7. The all-sky simulation has the highest minimum. This is consistent with the findings in EKE analysis. The largest differences

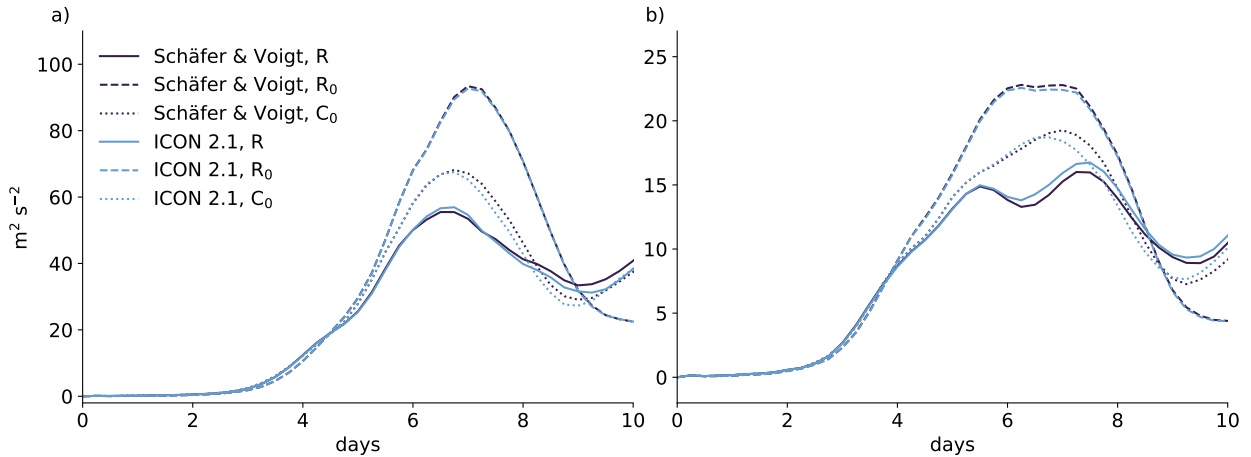


Figure 4.1: Global mean EKE at a) 300 hPa and b) 925 hPa throughout the life span of the cyclone for Schäfer and Voigt (2018) (dark) and ICON 2.1 (blue). EKE for the all-sky simulations (R) is shown by solid, the simulations without radiation (R₀) by dashed and clear-sky simulations (C₀) by dotted lines. Please note the different scales.

between ICON 2.0 and 2.1 appear in the clear-sky simulation, but even these differences are rather small compared to the differences between the three simulation setups.

Precipitation starts to form around day 2 in all-sky and clear-sky simulations, with a two-day delay for the simulation without radiation (Figure 4.3a). The total amount of precipitation is highest in all-sky simulations, producing more than 25 mm in the domain mean. The maximum values in clear-sky simulations are only slightly lower, reaching 24 mm on day 10. Both ICON versions show again only marginal differences starting around day 2, which rarely exceed $\pm 1\%$.

Total cloud cover in the domain mean starts evolving on day 1 in all-sky and clear-sky simulations. Clouds grow rapidly until day 2. The maximum cloud covers in all-sky simulations are slightly more than 80%, and around 70% in clear-sky simulations. Without active radiative heating, clouds do not evolve until day 2, growing slower and reaching the peak total cloud cover around day 7.

Large-scale radiative cooling emerging at the beginning in all-sky and clear-sky simulations (see Figure 3.5) leads to quicker saturation and, thus, sooner cloud formation than in the simulations without radiation. The high rates of condensational heating then lead to more precipitation. In contrast, the absence of radiative cooling during the first few days in the simulations without radiation leads to a later onset of precipitation.

The differences between ICON 2.0 and 2.1 simulations are negligible in all shown metrics, indicating that both model versions simulate the same cyclones. These findings legitimate the decision to use ICON 2.1 for further analyses. ICON 2.0 will not be used from this point onward in this thesis.

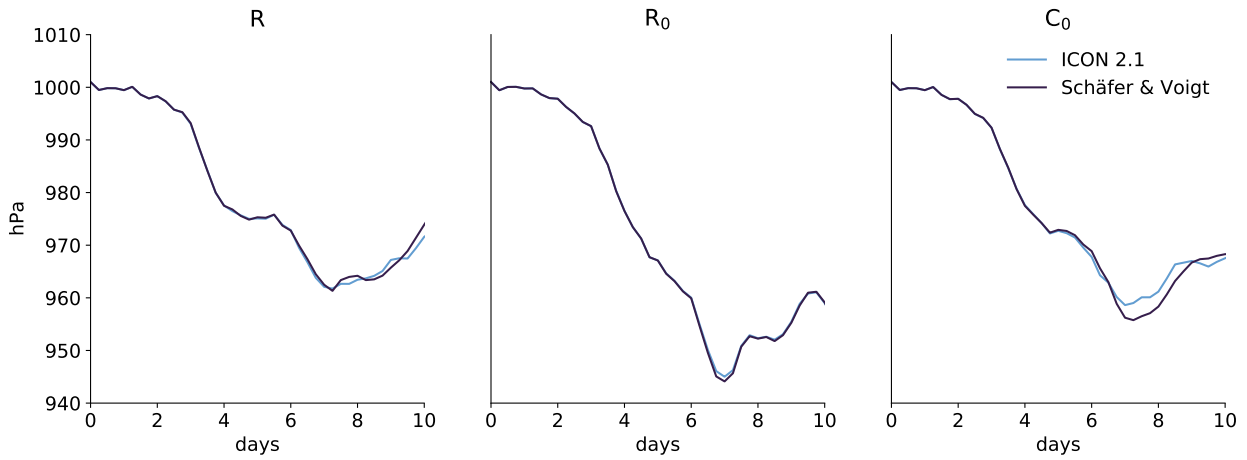


Figure 4.2: Minimum surface pressure by Schäfer and Voigt (2018) (dark) and ICON 2.1 (blue) throughout the life span of the cyclone for all-sky simulations (R), simulations without radiation (R_0), and clear-sky simulations (C_0).

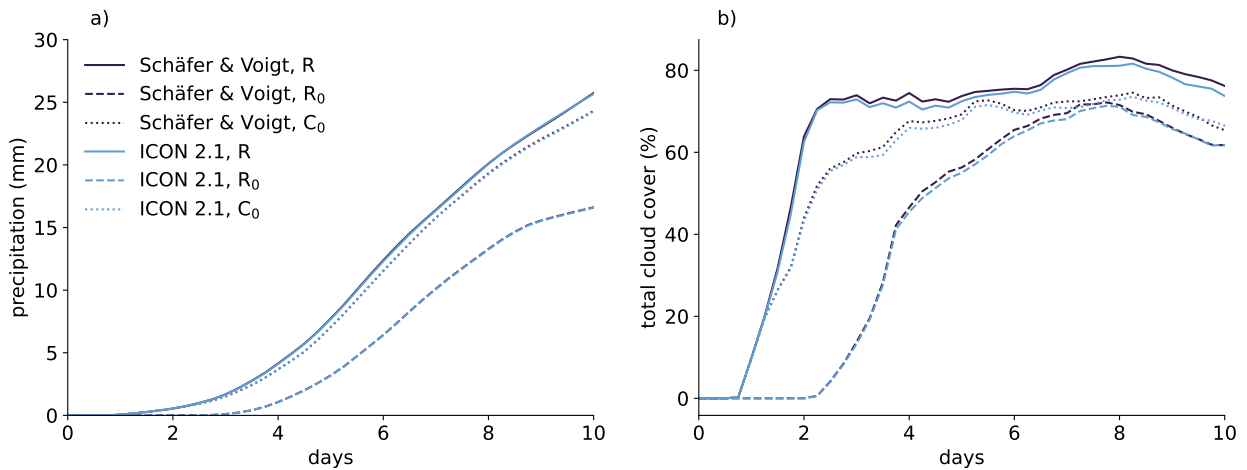


Figure 4.3: Domain mean of a) accumulated precipitation and b) total cloud cover throughout the life span of the cyclone in Schäfer and Voigt (2018) (dark) and ICON 2.1 (blue). All-sky simulations (R) are shown by solid, simulations without radiation (R_0) by dashed and clear-sky simulations (C_0) by dotted lines.

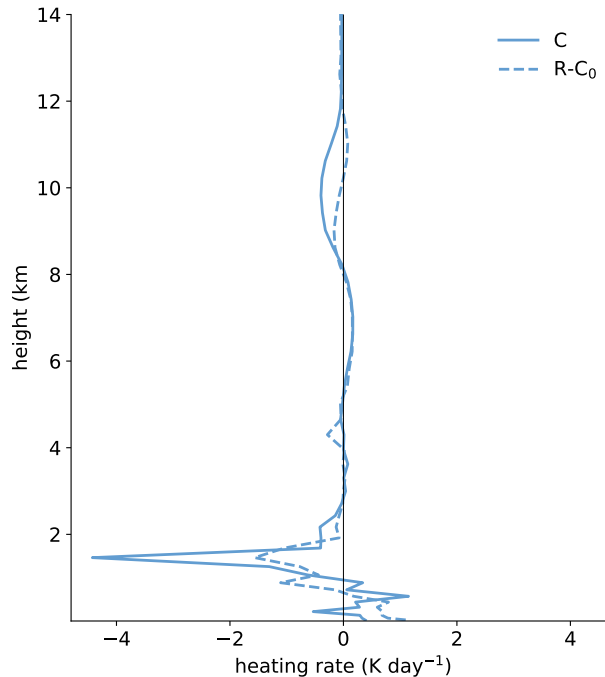


Figure 4.4: Vertical profile of domain mean cloud-radiative heating rates on day 6 in ICON 2.1, using heating rates from the simulation with CRH only (solid) and the difference of the heating rates in the all-sky and clear-sky simulations (dashed).

4.2 Isolating the impact of cloud-radiative heating with a new simulation approach

Since I can reproduce the results from Schäfer and Voigt (2018) with ICON 2.1, I can use it to apply a new simulation strategy, for which the cyclone interacts only with CRH (simulation C). This approach solves the issue of large initial radiative cooling raised in Schäfer and Voigt (2018) (see Section 3.3, Figure 3.5).

Simulation C outputs CRH directly, which means that the CRH impact on the cyclone does not have to be derived indirectly from all-sky and clear-sky simulations (see Figure 4.4), which was the case in the simulation strategy by Schäfer and Voigt (2018).

Using only CRH to heat the cyclone leads to a weakening of peak EKE in the upper and lower troposphere (Figure 4.5), qualitatively consistent with the CRH impact seen in Figure 4.1. The CRH impact obtained with CRH only is, however, less pronounced than the impact retrieved by the difference of all-sky and clear-sky simulations.

These differences in CRH impacts might arise from the initial radiative cooling in the all-sky and clear-sky simulation. Schäfer and Voigt (2018) analyzed MAPE and EKE as large-scale and small-scale energy reservoirs, respectively, to verify that the radiative weakening of the cyclone arises from cyclone scales (see Section 1.3). They argue that MAPE decreases in proportion to EKE increase, and they find only minor differences in the equilibrium of

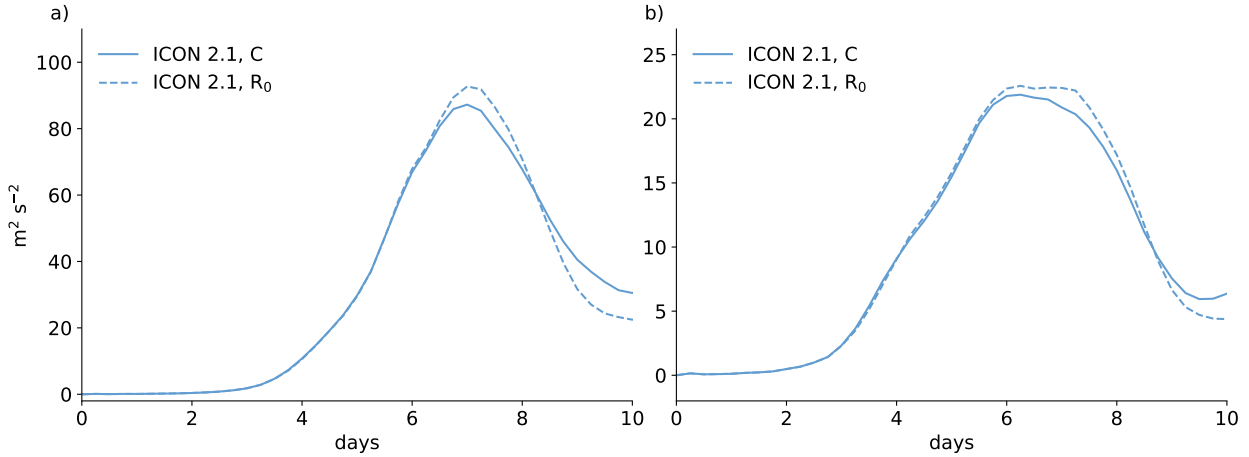


Figure 4.5: Global mean EKE at a) 300 hPa and b) 925 hPa throughout the life span of the cyclone in ICON 2.1. EKE for the simulation with CRH only (C) is shown by solid and the simulations without radiation (R_0) by dashed lines. Please note the different scales.

radiative cooling and convection. This indicates that the radiative processes work on the scale of the cyclone itself. However, they note that MAPE does not necessarily obtain other relevant large-scale parameters, for example the phase difference between upper- and low-level disturbances.

While minor changes in the Lorenz energy cycle and further large-scale parameters might be the reason for the difference in the extent of the CRH impact on EKE, the results of Schäfer and Voigt (2018) are qualitatively consistent with the new approach. Simulation C has the advantage of having only little initial radiative adjustment, ensuring clearer comparisons to the reference simulation. Therefore, the new simulation approach avoids the need to analyze MAPE.

4.3 Changes in the cloud-radiative heating impact with a new model version

The third model version I use in this thesis is ICON 2.6. This is the latest model version for operational use. The relevant differences to ICON 2.1 are described in Section 3.2. I will test the same analysis as in the Section 4.1 with ICON 2.6 and compare it to 2.1.

My main metric for cyclone strength, EKE, shows substantial differences in ICON 2.6 compared to ICON 2.1 (Figure 4.6). While ICON 2.1 showed a very similar EKE development as ICON 2.0, ICON 2.6 now produces different cyclones in terms of EKE.

Cyclone development starts around day 3, just as in ICON 2.1. EKE in simulation R in ICON 2.6, however, continues to grow beyond the analogous EKE values of ICON 2.1, resulting in a notably stronger and longer lasting cyclone. All-sky peak EKE in the upper troposphere in ICON 2.6 is 32% higher than in ICON 2.1. The cyclone in simulation R

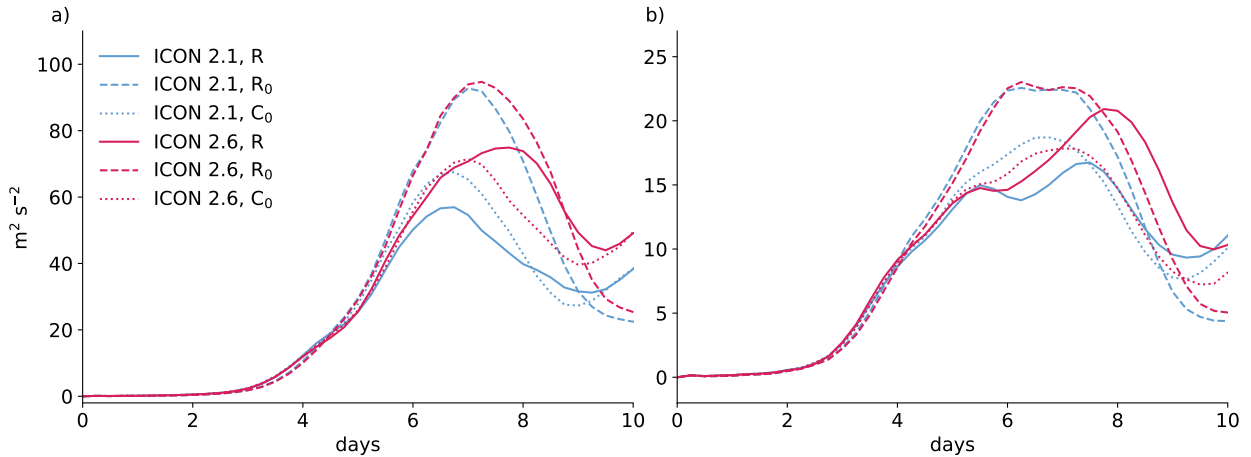


Figure 4.6: Global mean EKE at a) 300 hPa, corresponding to the upper troposphere, and b) 925 hPa, representing the lower troposphere, throughout the life span of the cyclone. Comparison between ICON 2.1 and ICON 2.6, marked by blue and pink colors, respectively. Simulations R use all-sky radiation, R_0 no radiation, and C_0 clear-sky radiation.

reaches its upper-tropospheric maximum on day 6 in ICON 2.1, while the cyclone grows until around day 8 in ICON 2.6.

Simulations R_0 have a similar intensification phase and similar peak EKE values, but with a slightly slower breakdown of upper-tropospheric EKE in ICON 2.6. Looking at the clear-sky simulations, the distinction between the model versions is rather small as well, even though there is already an indication that the simulated cyclones are not the same anymore. This might be due to differences in the microphysical heating rates.

While the runs with ICON 2.1 and 2.6 are fairly consistent as long as radiation is off or only clear-sky radiation is used, the results differ significantly when radiation is on. Overall, radiation still has a weakening impact on the cyclone strength. However, simulation R in ICON 2.6 shows a 7% stronger cyclone than simulation C_0 . In ICON 2.1, simulation R creates an even weaker cyclone than simulation C_0 . Since the clear-sky results almost look alike in both model versions, this indicates that differences arise from CRH rates.

The CRH impacts derived from all-sky and clear-sky simulations are consistent with the CRH impact obtained by simulation C (Figure 4.7). CRH weakens peak EKE at 300 hPa by 6% in ICON 2.1 and yet strengthens it by 6% in ICON 2.6. The impact is less pronounced in the lower troposphere, where CRH has barely an impact in ICON 2.6.

As for minimum surface pressure, ICON 2.6 simulations R and C_0 generate deeper cyclones than ICON 2.1 (Figure 4.8). The changes in minimum surface pressure between the model versions start occurring around day 5, thus during the cyclones' intensification phase. In simulation R, the cyclone's minimum surface pressure has lower values in ICON 2.6 than in ICON 2.1, indicating a deeper cyclone in ICON 2.6. Altogether, all-sky radiation has a weakening impact on minimum surface pressure in both model versions, which is marked by

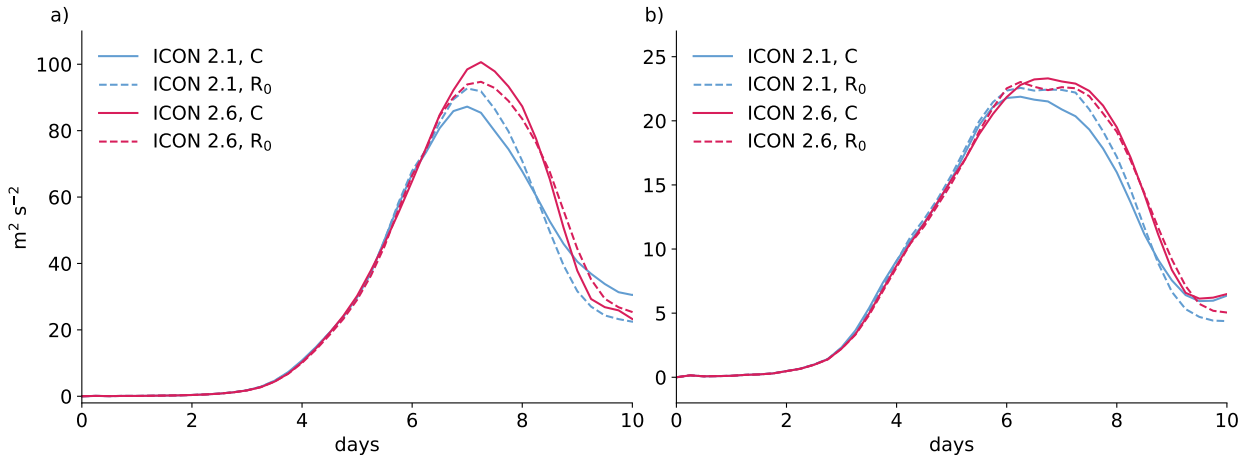


Figure 4.7: Global mean EKE at a) 300 hPa, corresponding to the upper troposphere, and b) 925 hPa, representing the lower troposphere, throughout the life span of the cyclone. Comparison between ICON 2.1 and ICON 2.6, marked by blue and pink colors, respectively. Simulations C use only cloud radiation and R_0 no radiation.

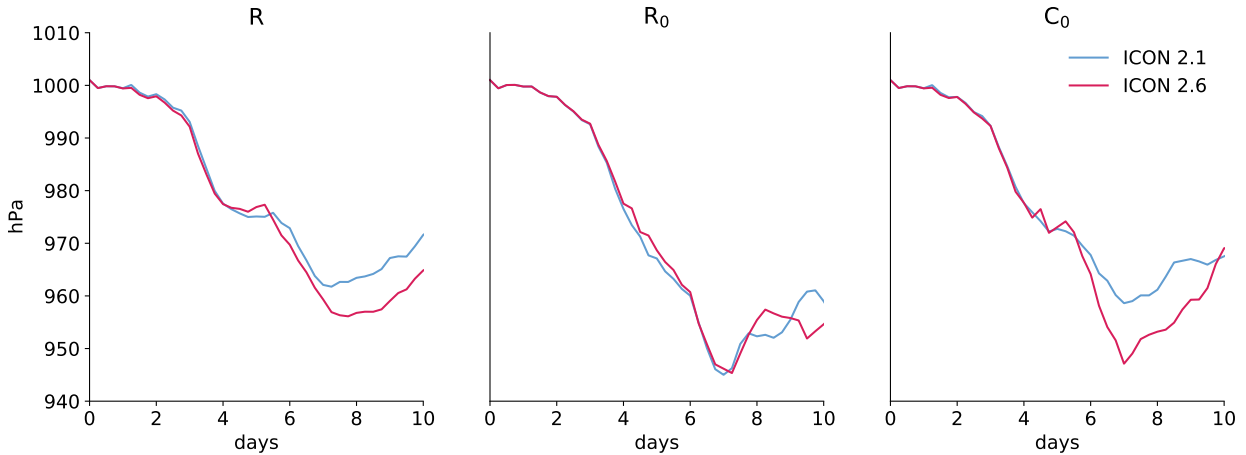


Figure 4.8: Comparison of minimum surface pressure in ICON 2.1 and 2.6 throughout the life span of the cyclone for simulations R, R_0 and C_0 .

the higher surface pressure minima compared to the results of simulation R_0 .

Due to the fact that simulations C_0 create deeper cyclones in terms of minimum surface pressure than simulations R, the cloud impact now appears robust across the two model versions. This is contrary to the findings regarding the clear-sky impact in the EKE analysis, because simulation C_0 in ICON 2.6 creates a weaker cyclone in terms of EKE compared to simulation R, but a deeper cyclone in terms of minimum surface pressure.

Only simulations R_0 show similar evolution of minimum surface pressure until the cyclone begins to recede again. The surface pressure minima of simulations R_0 are the lowest compared to the other simulations, which is consistent with the EKE analysis.

Accumulated precipitation is substantially lower in ICON 2.6 compared to ICON 2.1 (Figure 4.9). This could be related to lower surface heating fluxes in ICON 2.6. Simulation

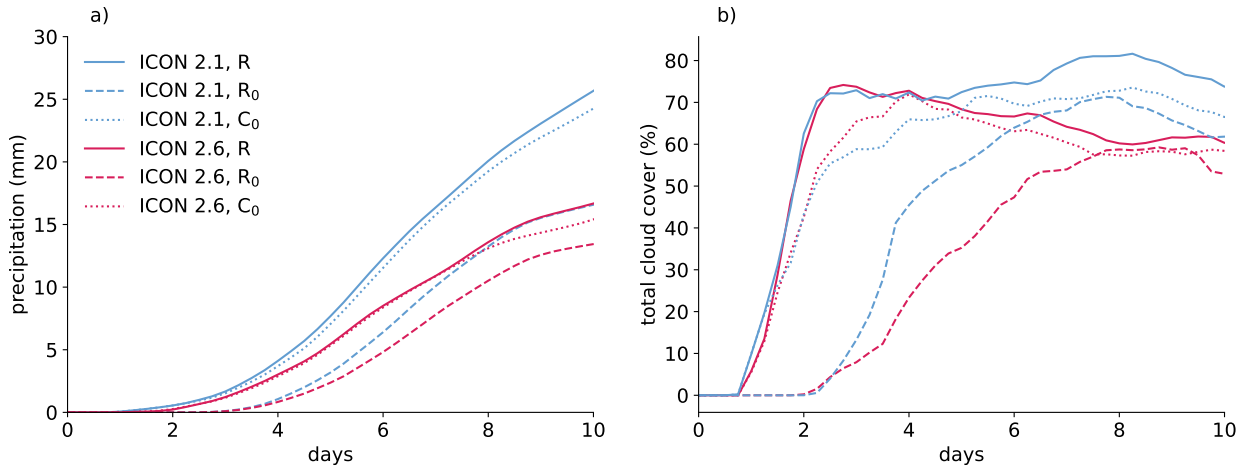


Figure 4.9: Domain mean of a) accumulated precipitation and b) total cloud cover throughout the life span of the cyclone in ICON 2.1 (blue) and ICON 2.6 (pink). R simulations are shown by solid, R₀ by dashed and C₀ by dotted lines.

R in ICON 2.6 reaches about the same accumulated precipitation as R₀ in ICON 2.1, which is the lowest maximum for ICON 2.1 simulations. In ICON 2.6, simulation C₀ produces the same precipitation amount as R until the cyclones reach their maximum strength around day 7. R₀ in ICON 2.6 produces the least precipitation throughout the lifespan of the cyclones. R and C₀ in ICON 2.1, on the other hand, evince the highest precipitation at all times.

In total, ICON 2.1 and ICON 2.6 show very different results for simulations with enabled radiation, especially all-sky radiation. The contradicting impacts on EKE apparently emerge from the presence of different CRH. The simulations without radiation, however, show very similar results for EKE and minimum surface pressure. Thus, I will look into the differences related to CRH between ICON 2.1 and 2.6.

4.4 Differences in clouds and radiative heating rates in the same large-scale environment

Since both model versions produce very similar cyclones while the interaction with radiation is prohibited, there is the advantage that I can investigate their differences for the same large-scale environment. The prior section showed how enabling cloud radiation resulted in different cyclone impacts. Therefore, looking into the cloud properties of the simulation without radiation could help understand the source of these differences.

Figure 4.10 shows the domain mean vertical profile of cloud water and ice content on day 6. The cyclones are already well developed on that day but have not reached their maximum EKE yet. While the cloud ice content shows no significant difference between ICON 2.1 and 2.6, the cloud water content varies strongly, especially in the boundary layer.

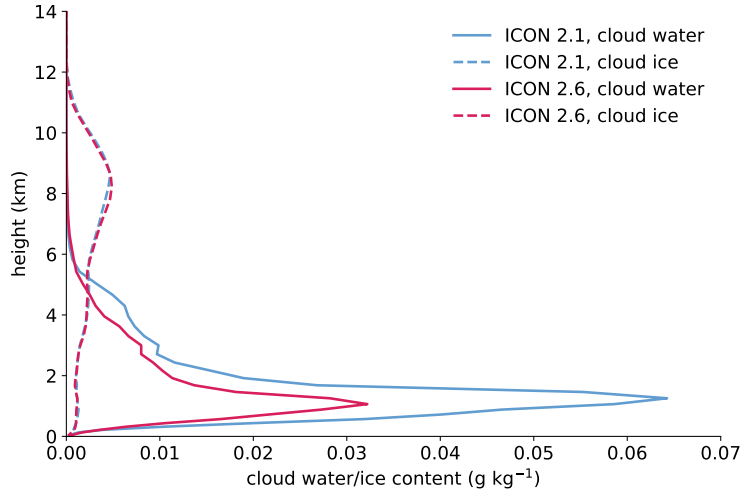


Figure 4.10: Vertical profile of domain mean cloud water content, depicted by solid lines, and cloud ice content, depicted by dashed lines, in the simulations without radiation (R_0) on day 6. Blue lines are for ICON 2.1 and pink lines for ICON 2.6.

The maximum cloud water content in ICON 2.6 is 0.033 g/kg, whereas the cloud water in ICON 2.1 reaches values up to 0.064 g/kg. Thus, the ICON 2.1 simulation produces twice as much cloud water in the boundary layer as ICON 2.6, but also above the boundary layer cloud water is substantially higher.

The simulations without radiation per definition prohibit radiation to interact with the cyclone, but Behrooz Keshtgar enabled the model to compute radiative heating rates and output them as a diagnostic so that I can compare them. This means that the radiation scheme is now active and stores radiative heating rates, but values of 0 are passed to the dynamical core instead of the actual heating rates. Therefore, the cyclone is still not interacting with radiative heating rates and is similar in both model versions, but I can use these heating rates for analysis. This helps me to understand where differences due to radiation would occur if radiation was allowed to interact with the cyclone. I call these heating rates “diagnostic” heating rates.

Figure 4.11 shows low-level clouds and net heating rates in the lower and upper troposphere on day 6 for the mean cyclone. The heating rates were obtained by subtracting diagnostic clear-sky from all-sky heating rates and averaging over altitudes corresponding to approximately 750-950 hPa and 250-350 hPa. The low-level cloud cover on day 6 is higher in ICON 2.1 than in ICON 2.6 (Figure 4.11a, b). The high-pressure area located in the southeastern section of the system is cloud-free in ICON 2.6, whereas ICON 2.1 produces clouds even in this area. Additionally, there is high cloud cover in the northernmost latitudes in 2.1, which is missing in 2.6. Overall, the low-level cloud field in ICON 2.6 is more or less limited to the warm conveyor belt and the low-pressure system.

Figure 4.11c-f further shows net diagnostic heating rates in the lower and upper tropo-

sphere on day 6. The upper troposphere is dominated by distinct cloud-radiative cooling in the warm conveyor belt, reaching values up to 10 K day^{-1} . Regions of the warm conveyor belt in the lower troposphere are characterized by modest cloud-radiative warming. Around the area of minimum surface pressure, low-level clouds radiatively cool the cyclone center. The most obvious difference appears in the high-pressure area in the lower troposphere, where ICON 2.1 produces cloud-radiative cooling whereas ICON 2.6 does not. This is consistent with the low-level cloud cover in Figure 4.11a, b.

The vertical structure of CRH is shown in Figure 4.12. In both model versions, the boundary layer is characterized by positive CRH below a layer of strong negative CRH. This cooling layer is located southward of the minimum surface pressure and is more pronounced in ICON 2.1, exceeding -10 K day^{-1} . At cloud top, longwave cooling dominates the net heating rates. The vertical structure is similar in ICON 2.1 and 2.6, although ICON 2.1 has stronger cooling in the boundary layer.

The differences in the diagnostic heating rates become even clearer when looking at their vertical profiles computed as domain means. Figure 4.13 shows shortwave, longwave, and net heating rates on day 6. Diagnostic all-sky shortwave and longwave radiative heating rate maxima are about twice as large in ICON 2.1 compared to 2.6. In clear-sky diagnostics, the differences are relatively small. The largest differences appear in the boundary layer below 2 km, both in all-sky and clear-sky heating rates.

The last row of Figure 4.13 shows the sole cloud contribution to radiative heating. Cloud-radiative heating/cooling within the boundary layer in ICON 2.1 is twice as strong compared to ICON 2.6, both in shortwave and longwave radiation. In terms of net effects, the ICON 2.1 simulation indicates cooling the cyclone's boundary layer by cloud radiation twice as much as in ICON 2.6.

Thus, the cyclones in the simulations without radiation are similar because of the absence of CRH. Diagnostic CRH within the boundary layer largely differs between ICON 2.1 and 2.6. The next chapter, therefore, focuses on the CRH impact on cyclone strength at certain height levels - using some new simulation strategies.

4.5 Competing impacts of clouds in the boundary layer and free troposphere

The boundary layer appears to be important for the overall CRH impact on cyclone strength. To examine the impact of boundary layer CRH in detail, I use new simulations that enable or disable the interaction of boundary layer CRH with the cyclone. Simulation C_{BL} heats the cyclone only with CRH within the boundary layer, whereas C_{FT} uses CRH only from the free troposphere. These simulations are described in more detail in Section 3.3.

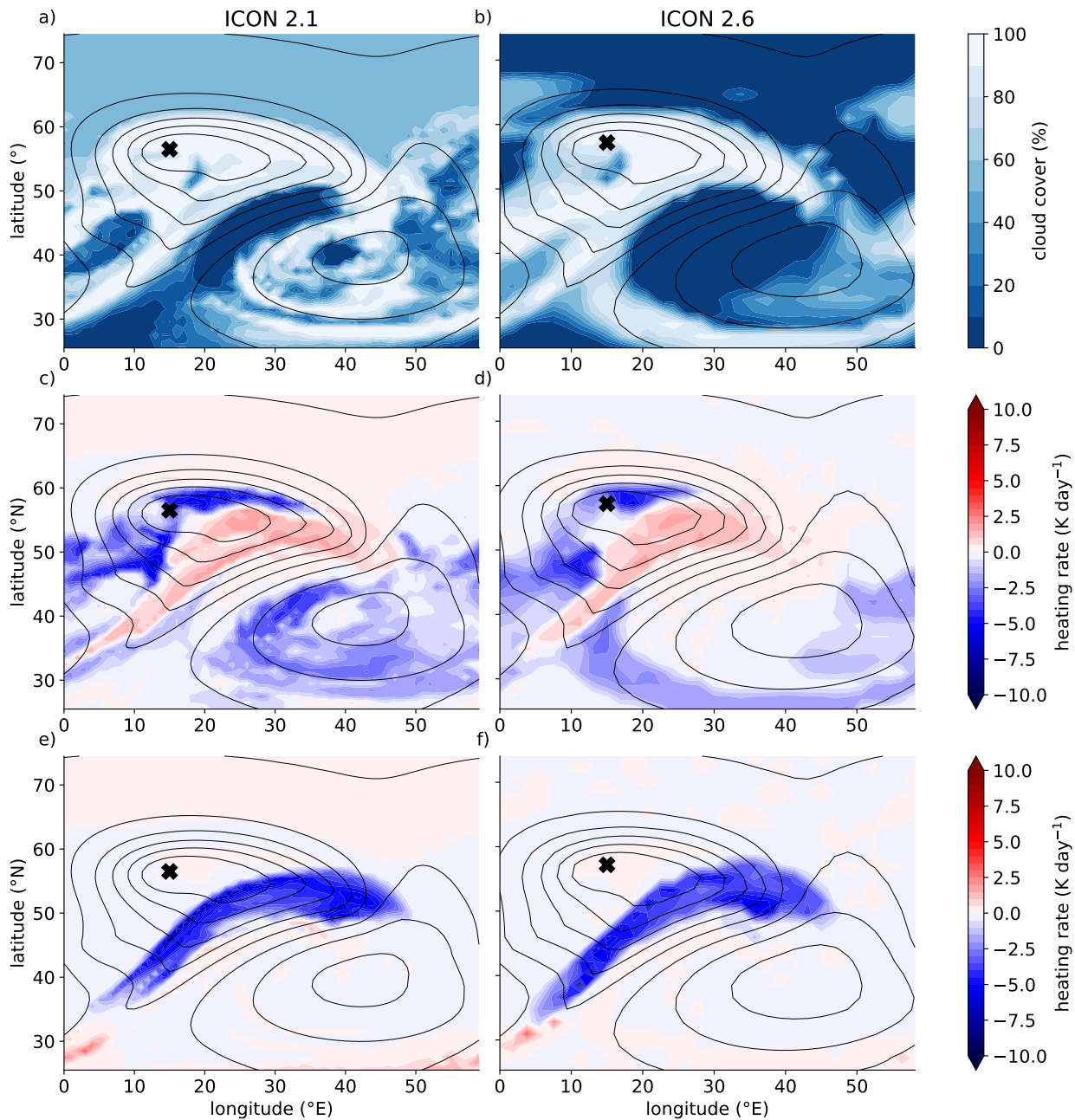


Figure 4.11: a, b) Comparison of low-level cloud cover on day 6 between ICON 2.1 and 2.6, obtained from simulations without radiation (R_0). c, d) Diagnostic net CRH averaged between height levels corresponding to approximately 750 hPa and 950 hPa, and to e, f) 250 hPa and 350 hPa in K day^{-1} . The contours show surface pressure and the cross marks the location of its minimum value. The fields are averaged over the six cyclones. The contour lines show the pressure field of the mean cyclone.

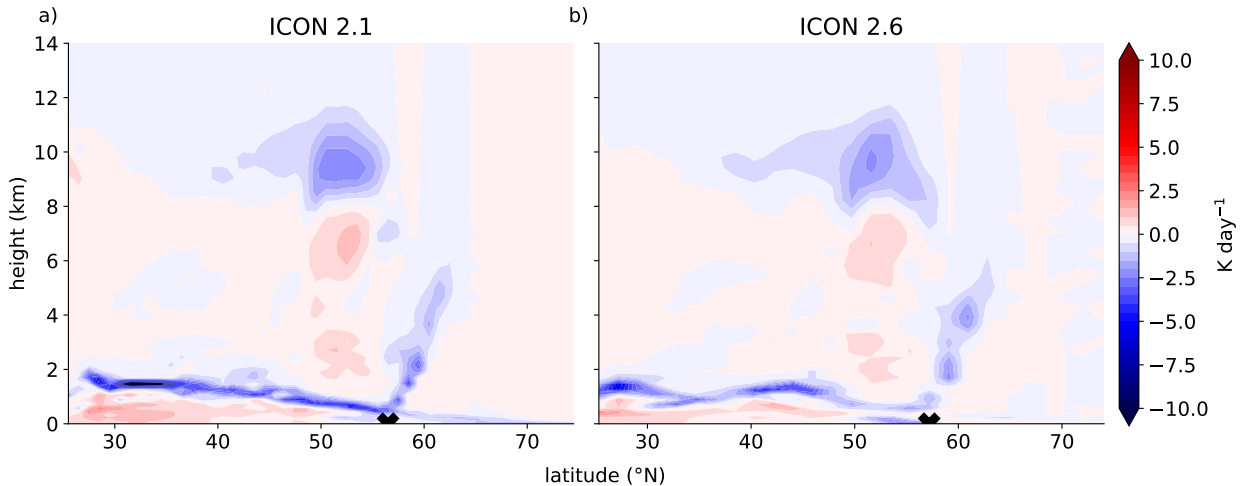


Figure 4.12: Zonal mean of diagnostic net cloud-radiative heating rate on day 6 obtained from simulations without radiation (R_0). The color shadings denote the net heating rates in K day^{-1} , The black “v” marks the location of minimum surface pressure.

Altering the levels where CRH is active leads to different evolution of EKE, as shown in Figure 4.14 at 300 hPa. All simulated cyclones evolve similarly in the beginning, starting to differ around day 6 - shortly before the cyclones’ peak stage of maturity. ICON 2.1 simulations C and C_{BL} generate very similar but the weakest cyclones in terms of EKE at 300 hPa.

In ICON 2.6, simulation C_{BL} has the lowest EKE values. However, every ICON 2.6 simulation has higher peak EKE at 300 hPa than its ICON 2.1 equivalent. Boundary layer CRH in ICON 2.6 creates an 8% stronger cyclone than in ICON 2.1. In terms of free-tropospheric CRH, ICON 2.6 creates a 6% stronger cyclone than ICON 2.1. This is consistent with the results of Section 4.2, where I concluded that CRH in ICON 2.1 creates lower peak EKE than ICON 2.6.

Yet, both model versions show the same impacts of boundary layer and free-tropospheric CRH. Free-tropospheric CRH generates the strongest cyclones, whereas boundary layer CRH creates the weakest cyclones in both model versions.

EKE results by simulation C in ICON 2.1 are very similar to those of simulation C_{BL} . Nevertheless, this is different in ICON 2.6, where EKE of simulation C resembles that of simulation C_{FT} . Due to the fact that simulation C has both boundary layer and free-tropospheric CRH enabled, the impacts of those seem to compete with each other.

The weakening impact of boundary layer CRH and the strengthening due to CRH in the free troposphere becomes even more evident when I extract the CRH impact on peak EKE, shown in Figure 4.15. The CRH impact is derived according to equations described in Section 3.4. By these combinations of the simulations, I can not only extract the CRH impact on EKE but also make statements about the robustness of these impacts due to the many simulations.

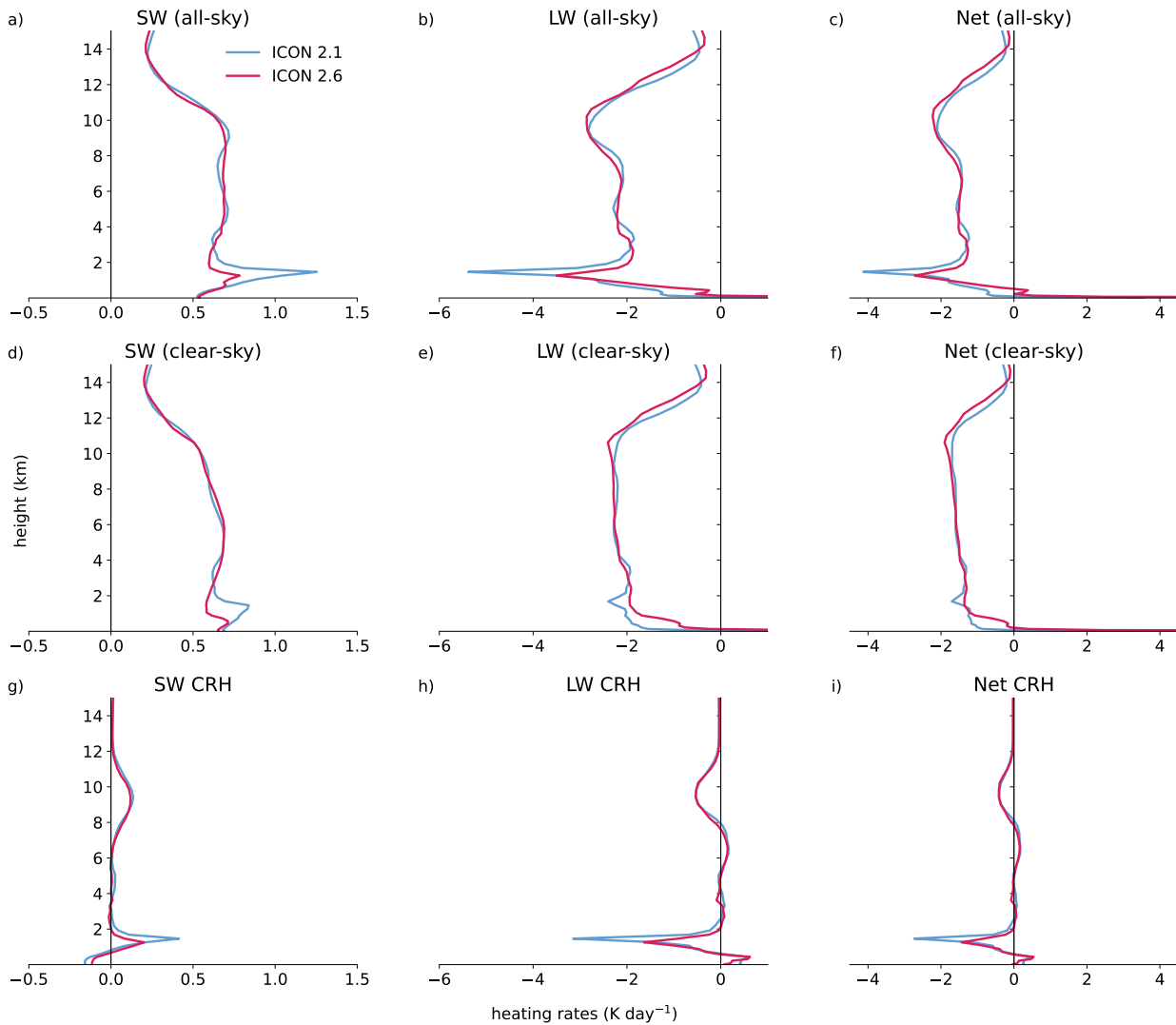


Figure 4.13: Vertical profiles of diagnostic heating rates obtained from simulations without radiation on day 6, showing a-c) diagnostic all-sky heating rates, d-f) diagnostic clear-sky heating rates, and g-i) cloud-radiative heating rates. All values are given in K day^{-1} . Please note the varying scales for heating rates of each column.

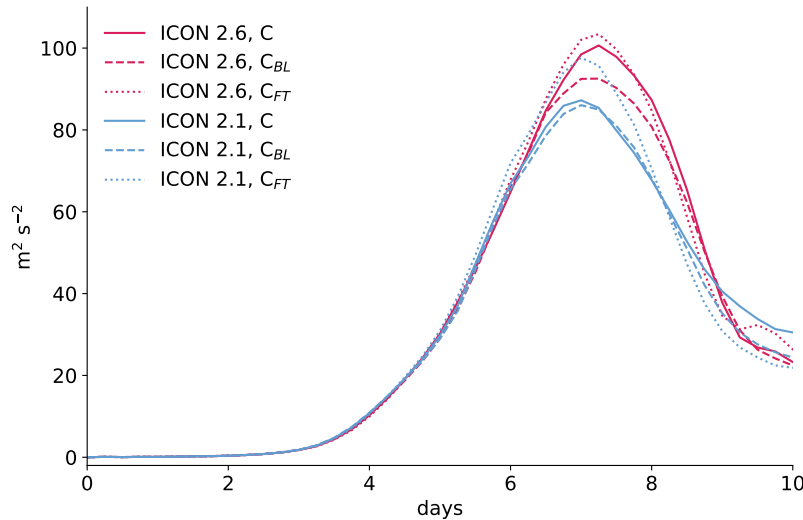


Figure 4.14: Temporal evolution of EKE at 300 hPa in simulations using CRH at all levels (C), only CRH in the boundary layer (C_{BL}), and free-tropospheric CRH (C_{FT}) to heat the cyclone.

The analysis method I use is described in more detail in Section 3.4.

The CRH impact in the boundary layer is given by $C_{BL}-R_0$ and $C-C_{FT}$. The weakening impact is more pronounced in ICON 2.1, ranging from -6.7 to -10.4 m^2s^{-2} . The values in ICON 2.6 are rather similar ($\text{EKE}_{BL,2.6} = -2.4$ $\text{m}^2\text{s}^{-2} \pm 0.3$ m^2s^{-2}).

In contrast to the boundary layer CRH weakening impact, CRH in the free troposphere strengthens the cyclone in both model versions. The impact contributions to peak EKE range from 1.2 m^2s^{-2} , which is the ICON 2.1 minimum, to 8.5 m^2s^{-2} , which is the ICON 2.6 maximum.

Since both model versions show the same impacts for boundary layer CRH and CRH in the free troposphere, respectively, these impacts are robust within my analysis.

Taking CRH at all altitudes into account, ICON 2.1 shows an overall weakening ranging from -5.5 to -10.6 m^2s^{-2} , while ICON 2.6 shows an overall strengthening of the cyclone with values around (5.3 ± 0.4) m^2s^{-2} . $R-C_0$ is the approach by Schäfer and Voigt (2018), which is added as a reference. Especially in ICON 2.6, their approach results in similar CRH impact as the new approach, which is $C-R_0$.

The overall CRH impact can also be estimated by two additional approaches, where I combine the simulations C_{BL} and C_{FT} with either R_0 or C . The results for the CRH impact on peak EKE at 300 hPa is depicted in Figure 4.16. This comparison shows that the overall impact of CRH remains robust within each model version: Overall weakening in ICON 2.1, strengthening in ICON 2.6.

However, there are some crucial differences regarding the extent of the CRH impact. While the CRH impact on peak EKE is nearly independent of the calculation approach, the

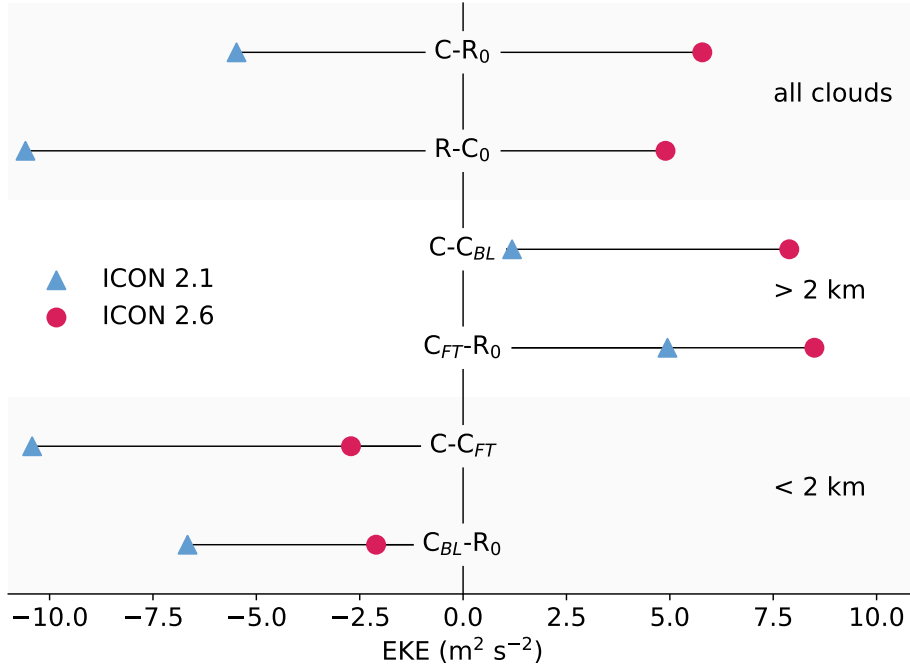


Figure 4.15: Cloud-radiative contribution to peak global-mean EKE at 300 hPa in m^2s^{-2} . The uppermost two rows show the overall CRH impact in terms of EKE in ICON 2.1 (blue triangles) and ICON 2.6 (pink circles). The two middle rows show the impact of CRH in the free troposphere alone, and the lower rows are the EKE impact of CRH within the boundary layer.

standard deviation in ICON 2.1 is approximately 6 times higher compared to ICON 2.6:

$$\text{EKE}_{2.6} = (5.6 \pm 0.6) \text{m}^2\text{s}^{-2}$$

$$\text{EKE}_{2.1} = (-6.8 \pm 3.5) \text{m}^2\text{s}^{-2}$$

The reason for the opposing CRH impacts on EKE between ICON 2.1 and 2.6 can be explained by the competing impacts of boundary layer and free-tropospheric CRH. ICON 2.1 simulations are dominated by low-level cloud cover, whose radiative heating weakens the cyclone. Due to this pronounced low-level cloud cover, the weakening by boundary layer CRH outweighs the strengthening impact of free-tropospheric CRH. In ICON 2.6, CRH in the free troposphere prevails the impact of boundary layer CRH and results in overall strengthening of the cyclone.

Thus, the resulting CRH impact depends on cloud distribution. Figure 4.17 shows the vertical profile of domain mean total cloud cover on day 6 for ICON 2.1 and ICON 2.6. ICON 2.1 generates not only more low-level clouds than ICON 2.6, but also more high-level clouds, even in the simulation without radiation.

Figure 4.17a shows how different the cloud cover of simulations C is below 2 km. While the total cloud cover in ICON 2.1 is about 27%, it barely exceeds 14% in ICON 2.6. This

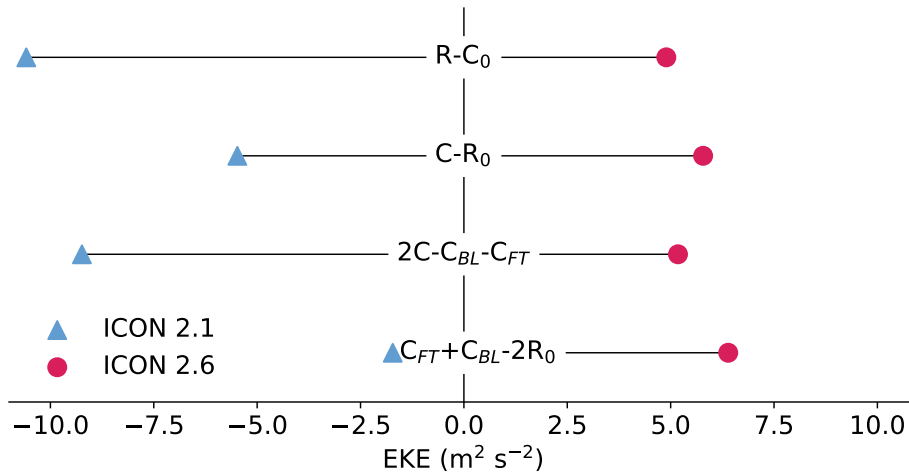


Figure 4.16: Overall CRH impact on peak global-mean EKE at 300 hPa in m^2s^{-2} in simulations with ICON 2.6 (pink circles) and simulations with ICON 2.1 (blue triangles). The respective calculation approach on isolating CRH is denoted by the abbreviations along the middle line, which are described in more detail in Section 3.4.

is consistent with the CRH rates discussed in Section 4.4. High-level clouds are also more pronounced in ICON 2.1, but low-level clouds govern the overall CRH impact. In ICON 2.6, the clouds above 2 km control the overall CRH impact, since the cloud cover below is not well enough pronounced.

When boundary layer CRH is enabled, cloud cover in both simulations C and C_{BL} , evolves similarly (Figure 4.17b). Additionally, the total cloud cover of simulation C_{FT} resembles that of the simulation without radiation. Due to these resemblances, free-tropospheric CRH has probably the best estimates of all impacts shown in Figure 4.15.

Boundary layer CRH weakening impact on cyclone strength is 3.5 times stronger in ICON 2.1 than in 2.6 by taking into account all simulation approaches. Strengthening of the cyclone due to CRH in the free troposphere is higher in ICON 2.6, and ICON 2.1 reaches only a third of the ICON 2.6 mean value. While these impacts are robust with respect to both model versions, the overall CRH is not. Overall, the impact of CRH on the cyclone depends on the cloud distribution, deciding which of the two competing impacts dominates the overall result. The total CRH impact on EKE is robust within each model version, regardless of the simulation approach.

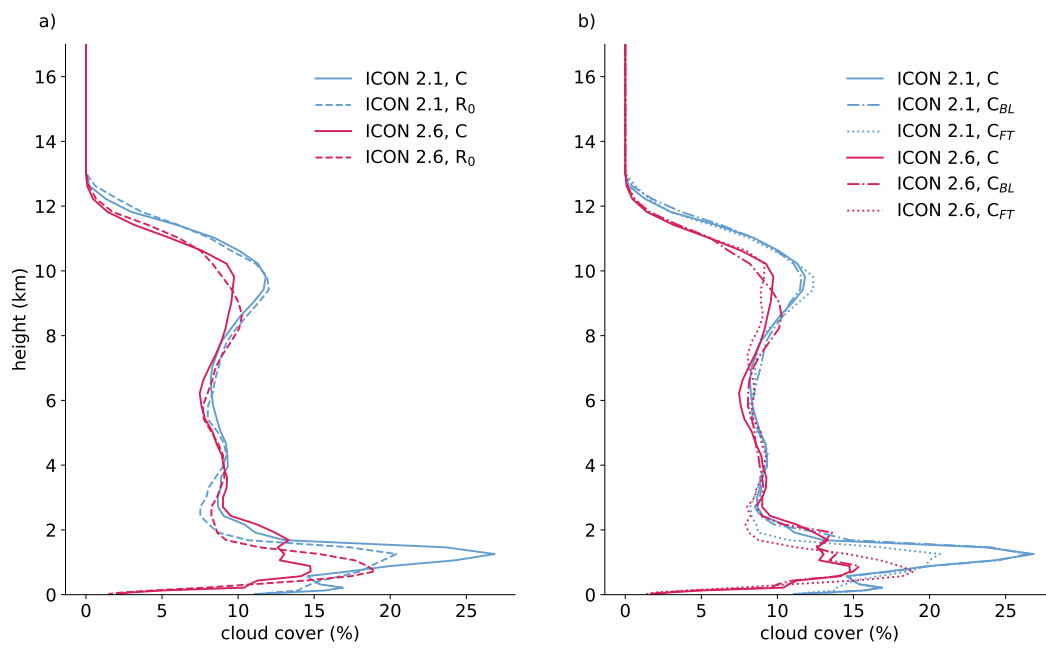


Figure 4.17: Vertical profile of the domain mean of total cloud cover in simulations a) C and R_0 , and b) C, C_{BL} and C_{FT} on day 6 for ICON 2.1 and 2.6.

5 | Conclusion

In this work I have studied the impact of cloud-radiative heating (CRH) on ETCs using idealized baroclinic life cycle simulations. Simulating ETCs in an idealized aquaplanet environment allows me to focus solely on atmospheric processes on the ETC, excluding other possibilities of where the desired impact could originate from.

The simulation strategy is based on Schäfer and Voigt (2018), but they had some weaknesses due to the initial radiative adjustment, which led to large-scale radiative cooling at the beginning of the simulations with all-sky radiation or clear-sky radiation. The radiative cooling did not appear in their simulation without radiation, and made their comparisons and interpretation of the results more complicated.

To make clear statements about the CRH impacts on cyclone strength, the simulation strategy is modified for this thesis. I use a new simulation strategy that heats the cyclone with CRH only. The new simulations have the advantage of preserving the mean state in which the cyclone evolves similar to simulation without radiation, leading to a clean comparison of simulations without radiation and those using only cloud radiation.

The attempt of reproducing the results by Schäfer and Voigt (2018) reveals that the overall CRH impact is not robust with respect to the model version. Simulations with ICON 2.1 produce weaker cyclones when cloud radiation is turned on compared to simulations without radiation, whereas simulations with ICON 2.6 generate stronger cyclones when cloud radiation interacts with the cyclone. These results are consistent with Schäfer and Voigt (2018) results, confirming that the initial radiative cooling in Schäfer and Voigt (2018) does not affect their general conclusions.

Moreover, the overall cloud-radiative weakening of peak EKE in ICON 2.1 can be observed in every set of simulations. The extent of the CRH impact, however, varies largely and ranges from $-1.7 \text{ m}^2\text{s}^{-2}$ to $-10.6 \text{ m}^2\text{s}^{-2}$. The strengthening impact of CRH on peak EKE in ICON 2.6 is robust across all simulation sets, and is rather similar in all approaches of isolating the CRH impact.

In Section 4.2, I argued that the disparity between the magnitude of the CRH impact on EKE derived by all-sky and clear-sky simulations, and by simulations with CRH only and without radiation, could stem from the differences in the initial radiative adjustment. Since the CRH impacts in ICON 2.6 are fairly similar, the argument does not hold for ICON 2.6.

Therefore, the reason for the disparity appears to originate from the ICON 2.1 model version itself.

In contrast to the overall CRH impact, the impact of clear-sky radiation is robust regarding the examined model versions. Clear-sky radiation has a weakening impact on cyclone strength and shows only small differences in EKE, which might arise from different micro-physical heating rates.

The second question that I address in this thesis is whether clouds at different altitudes impact the cyclone differently. To examine altitude dependence, I use two additional simulations in which I isolate CRH within the boundary layer and in the free troposphere, respectively.

The decomposition of boundary layer CRH and free-tropospheric CRH is motivated by the fact that the largest differences between ICON 2.1 and 2.6 heating rates appear in the boundary layer, pointing to uncertainty in boundary layer clouds. Altering the simulations without radiation so that the model also outputs “diagnostic” heating rates reveals that ICON 2.1 heating rates are twice as large as ICON 2.6 heating rates in the boundary layer.

A likely reason for the large radiative flux differences in the boundary layer is to the so-called “ c_p/c_v bug” which was fixed in ICON 2.6 (Zängl and Schäfer, 2021). Thus, the turbulence scheme in ICON 2.1 creates larger surface fluxes, leading to higher generation of low-level clouds and larger CRH in the boundary layer.

Further simulations reveal the competing impacts of boundary layer CRH and free-tropospheric CRH. Boundary layer CRH weakens the cyclone in terms of peak EKE, while CRH in the free troposphere has a strengthening impact on peak EKE. These impacts are found in both ICON 2.1 and 2.6 and are therefore robust with respect to the model version and to the simulation approach.

Nevertheless, the extent of these competing impacts differs between ICON 2.1 and 2.6. Boundary layer CRH in ICON 2.1 affects EKE 3-4 times more than to ICON 2.6. CRH in the free troposphere has a stronger impact in ICON 2.6.

The strengthening of EKE due to free-tropospheric CRH is consistent with the enhanced EKE in the extratropical upper-troposphere-lower stratosphere region due to ACRE (Li et al., 2015). Li et al. (2015) also found that ACRE decreases static stability near the tropopause and increases static stability at lower tropospheric levels. This appears to be consistent with my findings of cyclone strengthening due to CRH in the free troposphere and weakening at lower levels.

The overall CRH impact, therefore, is governed by the competition of CRH in the boundary layer and free troposphere. Thus, correct representation of cloud distribution in the mid-latitudes is an important factor for ETC development. However, vertical cloud distribution is often misrepresented compared to satellite observations (Naud et al., 2010; Field et al., 2011).

It is yet unclear if the competing impacts of CRH in different altitudes can be found in other models and radiation schemes as well. The decomposition in boundary layer and free-tropospheric CRH is rather coarse as I only split CRH into these two groups. It might be interesting to examine CRH over smaller sections of the troposphere. Furthermore, I only provide the diagnostic observations of CRH impacts on the ETC's intensity, but these results call for a dynamical argument explaining the mechanisms of cyclone strengthening or weakening due to CRH.

Since ETCs govern the daily weather in the midlatitudes, implementing realistic cloud-radiative fluxes and, thus, realistic CRH could help improving cyclone forecasts in operating NWP. Another task for future studies is testing my statements in realistic NWP setups.

The findings of the competing impacts of boundary layer and free-tropospheric CRH could help narrowing the cloud bias for cyclone representation in the Southern Ocean in climate models (e.g. Williams et al., 2013). Even though cloud uncertainty in the climate models used in IPCC AR6 decreased by 50% compared to AR5, clouds remain the largest contributor to the overall climate feedback uncertainty (Arias et al., 2021), and could result in biased cyclone representation. Moreover, global climate models tend to generate too small CRE in the extratropics (Klein and Jakob, 1999; Naud et al., 2010; Field et al., 2011; Bodas-Salcedo et al., 2012; Booth et al., 2013a; Williams et al., 2013), probably affecting cyclone representation as well.

The competing impacts of boundary layer and free-tropospheric CRH on ETC strength are a key novelty, emphasizing the importance of understanding the impacts of cloud processes and call for further studies on CRH impacts on cyclones.

Bibliography

- P. Arias, N. Bellouin, E. Coppola, R. Jones, G. Krinner, J. Marotzke, V. Naik, M. Palmer, G.-K. Plattner, J. Rogelj, M. Rojas, J. Sillmann, T. Storelvmo, P. Thorne, B. Trewin, K. Rao, B. Adhikary, R. Allan, K. Armour, G. Bala, R. Barimalala, S. Berger, J. Canadell, C. Cassou, A. Cherchi, W. Collins, W. Collins, S. Connors, S. Corti, F. Cruz, F. Dentener, C. Dereczynski, A. Luca, A. Niang, F. Doblas-Reyes, A. Dosio, H. Douville, F. Engelbrecht, V. Eyring, E. Fischer, P. Forster, B. Fox-Kemper, J. Fuglestvedt, J. Fyfe, N. Gillett, L. Goldfarb, I. Gorodetskaya, J. Gutierrez, R. Hamdi, E. Hawkins, H. Hewitt, P. Hope, A. Islam, C. Jones, D. Kaufman, R. Kopp, Y. Kosaka, J. Kossin, S. Krakovska, J.-Y. Lee, J. Li, T. Mauritsen, T. Maycock, M. Meinshausen, S.-K. Min, P. Monteiro, T. Ngo-Duc, F. Otto, I. Pinto, A. Pirani, K. Raghavan, R. Ranasinghe, A. Ruane, L. Ruiz, J.-B. Sallée, B. Samset, S. Sathyendranath, S. Seneviratne, A. Sörensson, S. Szopa, I. Takayabu, A.-M. Tréguier, B. Hurk, R. Vautard, K. Schuckmann, S. Zaehle, X. Zhang, and K. Zickfeld. Technical summary. In V. Masson-Delmotte, P. Zhai, A. Pirani, S. Connors, C. Péan, S. Berger, N. Caud, Y. Chen, L. Goldfarb, M. Gomis, M. Huang, K. Leitzell, E. Lonnoy, J. Matthews, T. Maycock, T. Waterfield, O. Yelekçi, R. Yu, and B. Zhou, editors, *Climate Change 2021: The Physical Science Basis. Contribution of Working Group I to the Sixth Assessment Report of the Intergovernmental Panel on Climate Change*, pages 33–144. Cambridge University Press, Cambridge, United Kingdom and New York, NY, USA, 2021. doi: 10.1017/9781009157896.002.
- P. Bechtold, M. Köhler, T. Jung, F. Doblas-Reyes, M. Leutbecher, M. J. Rodwell, F. Vitart, and G. Balsamo. Advances in simulating atmospheric variability with the ECMWF model: From synoptic to decadal time-scales. *Quarterly Journal of the Royal Meteorological Society*, 134(634):1337–1351, 2008.
- J. Bjerknes. *Life cycle of cyclones and the polar front theory of atmospheric circulation*. Geofysiske publikationer ; 3, 1. Kristiania, 1922.
- A. Bodas-Salcedo, K. Williams, P. Field, and A. Lock. The Surface Downwelling Solar Radiation Surplus over the Southern Ocean in the Met Office Model: The Role of Midlatitude Cyclone Clouds. *Journal of Climate*, 25(21):7467–7486, 2012.

- J. F. Booth, C. M. Naud, and A. D. Del Genio. Diagnosing Warm Frontal Cloud Formation in a GCM: A Novel Approach Using Conditional Subsetting. *Journal of Climate*, 26(16):5827–5845, 2013a.
- J. F. Booth, S. Wang, and L. Polvani. Midlatitude storms in a moister world: lessons from idealized baroclinic life cycle experiments. *Climate Dynamics*, 41(3):787–802, 2013b.
- I. A. Boutle, S. E. Belcher, and R. S. Plant. Moisture transport in midlatitude cyclones. *Quarterly Journal of the Royal Meteorological Society*, 137(655):360–373, 2011.
- D. Büeler and S. Pfahl. Potential vorticity diagnostics to quantify effects of latent heating in extratropical cyclones. Part I: Methodology. *Journal of the Atmospheric Sciences*, 74(11):3567–3590, 2017.
- J. L. Catto. Extratropical cyclone classification and its use in climate studies. *Reviews of Geophysics (1985)*, 54(2):486–520, 2016.
- J. L. Catto, C. Jakob, G. Berry, and N. Nicholls. Relating global precipitation to atmospheric fronts. *Geophysical Research Letters*, 39(10), 2012.
- J. M. Chagnon, S. L. Gray, and J. Methven. Diabatic processes modifying potential vorticity in a North Atlantic cyclone. *Quarterly Journal of the Royal Meteorological Society*, 139(674):1270–1282, 2013.
- W. R. Cotton, G. Bryan, and S. C. van den Heever. The Mesoscale Structure of Extratropical Cyclones and Middle and High Clouds. In *International Geophysics*, volume 99, pages 527–672. Elsevier Science & Technology, 2011.
- DKRZ. DKRZ User Portal: Mistral. <https://www.dkrz.de/up/systems/mistral>. accessed on 28.12.2021.
- G. Doms, J. Förstner, E. Heise, H.-J. Herzog, D. Mironov, M. Raschendorfer, T. Reinhardt, B. Ritter, R. Schrodin, S. J.-P., and G. Vogel. A Description of the Nonhydrostatic Regional COSMO Model. Part II: Physical Parameterization. Technical report, Consortium for Small-Scale Modelling, 2011. <http://www.cosmo-model.org>.
- E. T. Eady. Long Waves and Cyclone Waves. *Tellus*, 1(3):33–52, 1949.
- P. R. Field, A. Bodas-Salcedo, and M. E. Brooks. Using model analysis and satellite data to assess cloud and precipitation in midlatitude cyclones. *Quarterly Journal of the Royal Meteorological Society*, 137(659):1501–1515, 2011.
- A. H. Fink, S. Pohle, J. G. Pinto, and P. Knippertz. Diagnosing the influence of diabatic processes on the explosive deepening of extratropical cyclones. *Geophysical Research Letters*, 39(7), 2012.

- A. E. Gill. *Atmosphere-Ocean Dynamics*. Number v. 30 in International Geophysics Series. Academic Press, 1982.
- K. M. Grise, B. Medeiros, J. J. Benedict, and J. G. Olson. Investigating the Influence of Cloud Radiative Effects on the Extratropical Storm Tracks. *Geophysical Research Letters*, 46(13):7700–7707, 2019.
- K. F. Haualand and T. Spengler. Direct and indirect effects of surface fluxes on moist baroclinic development in an idealized framework. *Journal of the Atmospheric Sciences*, 77(9):3211–3225, 2020.
- J. R. Holton. *An introduction to dynamic meteorology*. International geophysics series; vol. 88. Elsevier, Amsterdam; London, 4th ed. edition, 2004.
- B. J. Hoskins and N. V. West. Baroclinic Waves and Frontogenesis. Part II: Uniform Potential Vorticity Jet Flows-Cold and Warm Fronts. *Journal of the Atmospheric Sciences*, 36(9):1663–1680, 1979.
- B. J. Hoskins, M. E. McIntyre, and A. W. Robertson. On the use and significance of isentropic potential vorticity maps. *Quarterly Journal of the Royal Meteorological Society*, 111(470):877–946, 1985.
- M. Kaviani, F. Ahmadi-Givi, A. R. Mohebalhojeh, and D. Yazgi. An assessment of radiative impacts of CO₂ on baroclinic instability using idealized life cycles. *Quarterly Journal of the Royal Meteorological Society*, 148(743):891–906, 2022.
- S. A. Klein and C. Jakob. Validation and sensitivities of frontal clouds simulated by the ECMWF model. *Monthly Weather Review*, 127(10):2514–2531, 1999.
- Y. Li, D. W. Thompson, and S. Bony. The Influence of Atmospheric Cloud Radiative Effects on the Large-Scale Atmospheric Circulation. *Journal of Climate*, 28(18):7263–7278, 2015.
- E. N. Lorenz. Available Potential Energy and the Maintenance of the General Circulation. *Tellus*, 7(2):157–167, 1955.
- E. J. Mlawer, S. J. Taubman, P. D. Brown, M. J. Iacono, and S. A. Clough. Radiative transfer for inhomogeneous atmospheres: RRTM, a validated correlated-k model for the longwave. *Journal of Geophysical Research: Atmospheres*, 102(D14):16663–16682, 1997.
- C. M. Naud, A. D. Del Genio, M. Bauer, and W. Kovari. Cloud vertical distribution across warm and cold fronts in CloudSat-CALIPSO data and a general circulation model. *Journal of Climate*, 23(12):3397–3415, 2010.

- J. P. Peixóto and A. H. Oort. Physics of climate. *Reviews of Modern Physics*, 56(3): 365–429, 1984.
- L. M. Polvani and J. G. Esler. Transport and mixing of chemical air masses in idealized baroclinic life cycles. *Journal of Geophysical Research: Atmospheres*, 112(D23), 2007.
- D. J. Posselt, G. L. Stephens, and M. Miller. CLOUDSAT: Adding a New Dimension to a Classical View of Extratropical Cyclones. *Bulletin of the American Meteorological Society*, 89(5):599–609, 2008.
- F. Prill, D. Reinert, D. Rieger, G. Zängl, J. Schröter, J. Förstner, S. Werchner, M. Weimer, R. Ruhnke, and B. Vogel. ICON Model Tutorial. Working with the ICON Model. Practical Exercises for NWP Mode and ICON-ART. Technical report, DWD, April 2019. https://code.mpimet.mpg.de/attachments/download/19568/ICON_tutorial_2019.pdf, accessed on 28.12.2021.
- D. M. Schultz, D. Keyser, and L. F. Bosart. The effect of large-scale flow on low-level frontal structure and evolution in midlatitude cyclones. *Monthly Weather Review*, 126(7):1767–1791, 1998.
- S. A. K. Schäfer and A. Voigt. Radiation Weakens Idealized Midlatitude Cyclones. *Geophysical Research Letters*, 45(6):2833–2841, 2018.
- M. A. Shapiro and D. Keyser. *Fronts, Jet Streams and the Tropopause*, pages 167–191. American Meteorological Society, Boston, MA, 1990.
- A. P. Siebesma, S. Bony, C. Jakob, and B. Stevens. *Clouds and Climate: Climate Science’s Greatest Challenge*. University of Cambridge ESOL Examinations, Cambridge, 2020.
- E. Spreitzer, R. Attinger, M. Boettcher, R. Forbes, H. Wernli, and H. Joos. Modification of Potential Vorticity near the Tropopause by Nonconservative Processes in the ECMWF Model. *Journal of the Atmospheric Sciences*, 76(6):1709–1726, 2019.
- M. T. Stoelinga. A potential vorticity-based study of the role of diabatic heating and friction in a numerically simulated baroclinic cyclone. *Monthly Weather Review*, 124(5): 849–874, 1996.
- K. Swanson. Extratropical Atmospheric Circulations. In *Handbook of Weather, Climate, and Water*, pages 39–56. John Wiley & Sons, Inc, Hoboken, NJ, USA, 2003.
- C. Thorncroft, B. Hoskins, and M. McIntyre. Two Paradigms of Baroclinic-Wave Life-Cycle Behavior. *Quarterly Journal of the Royal Meteorological Society*, 119:17 – 55, 01 1993. doi: 10.1002/qj.49711950903.

- G. Tselioudis and W. B. Rossow. Climate feedback implied by observed radiation and precipitation changes with midlatitude storm strength and frequency. *Geophysical Research Letters*, 33(2), 2006.
- O. Watt-Meyer and D. M. W. Frierson. Local and Remote Impacts of Atmospheric Cloud Radiative Effects Onto the Eddy-Driven Jet. *Geophysical Research Letters*, 44(19): 10,036–10,044, 2017.
- K. D. Williams, A. Bodas-Salcedo, M. Déqué, S. Fermepin, B. Medeiros, M. Watanabe, C. Jakob, S. Klein, C. Senior, and D. Williamson. The Transpose-AMIP II Experiment and Its Application to the Understanding of Southern Ocean Cloud Biases in Climate Models. *Journal of Climate*, 26(10):3258–3274, 2013.
- D. L. Williamson, M. Blackburn, B. J. Hoskins, K. Nakajima, W. Ohfuchi, Y. O. Takahashi, M. Ishiwatari, J. L. McGregor, H. Borth, V. Wirth, H. Frank, P. Bechtold, N. P. Wedi, H. Tomita, M. Satoh, M. Zhao, I. M. Held, M. J. Suarez, M.-I. Lee, M. Watanabe, M. Kimoto, Y. Liu, Z. Wang, A. Molod, K. Rajendran, A. Kitoh, and R. Stratton. The APE atlas. Technical report, 11 2012.
- J. E. Zimmerman, P. J. Smith, and D. R. Smith. The role of latent heat release in the evolution of a weak extratropical cyclone. *Monthly Weather Review*, 117(5):1039–1057, 1989.
- G. Zängl and S. Schäfer. Operational NWP System. Model configuration upgrade of ICON. Technical report, 04 2021.
https://www.dwd.de/DE/fachnutzer/forschung_lehre/numerische_wettervorhersage/nwv_aenderungen/_functions/DownloadBox_modellaenderungen/icon/pdf_2021/pdf_icon_14_04_2021.pdf?__blob=publicationFile&v=3, accessed on 27.04.2022.
- G. Zängl, D. Reinert, P. Rípodas, and M. Baldauf. The ICON (ICOsahedral Non-hydrostatic) modelling framework of DWD and MPI-M: Description of the non-hydrostatic dynamical core. *Quarterly Journal of the Royal Meteorological Society*, 141(687):563–579, 2015.

List of Figures

1.1	Conceptual models of Extratropical cyclones	8
1.2	Conveyor belt model, schematic	9
1.3	CloudSat observed extratropical cyclone	10
1.4	PV-induced cyclogenesis	10
1.5	The most unstable Eady wave	12
1.6	Vertical cross section of an ETC showing individual PV contributions	14
1.7	Impact of latent heat release on ETCs	15
1.8	Radiative heating profile in an ETC	19
1.9	Changes in temperature, zonal wind, radiative heating and latent heating	20
1.10	MAPE and EKE of idealized ETCs	21
3.1	Ertel potential vorticity in BLC type 1 and 2	24
3.2	LC1 and LC2, initial conditions	25
3.3	Initial temperature perturbation	26
3.4	Cyclone evolution, ICON 2.6	27
3.5	Temperature and wind change by day 3, ICON 2.6	29
3.6	C , C_{FT} and C_U CRH demonstration	30
3.7	Demonstration of mean cyclone analysis	31
3.8	Zonal mean EKE	32
4.1	EKE comparison: ICON 2.0 and 2.1	35
4.2	Comparison of minimum surface pressure in ICON 2.0 and 2.1	36
4.3	Comparison of total precipitation in ICON 2.0 and 2.1	36
4.4	ICON 2.1 heating rates	37
4.5	EKE in ICON 2.1, simulations R_0 and C	38
4.6	EKE comparison: ICON 2.1 and 2.6	39
4.7	EKE comparison: ICON 2.1 and 2.6, simulation C	40
4.8	Comparison of minimum surface pressure in ICON 2.1 and 2.6	40
4.9	Total precipitation and cloud cover in ICON 2.1 and 2.6	41
4.10	R_0 cloud water and cloud ice	42

4.11	R_0 low-level cloud cover and CRH	44
4.12	R_0 diagnostic heating rates (vertical)	45
4.13	R_0 diagnostic heating rates (domain mean)	46
4.14	EKE in simulations C, C_{BL} , and C_{FT}	47
4.15	Cloud-radiative contribution to peak global-mean EKE	48
4.16	Overall CRH impact on peak global-mean EKE	49
4.17	Total cloud cover (domain mean, vertical profile)	50

Acknowledgments

It turns out that writing a master's thesis during a pandemic is not so easy after all. For a long time, we students could hardly come to the university - nevertheless, Aiko Voigt and Behrooz Keshtgar managed to support me in the best possible way, even remotely. When I had questions, they always answered them very quickly. Aiko not only welcomed me into his group and showed me how real scientific working looks like, but also took the pressure off the writing process by always emphasizing that writing is an iterative process. A first draft is not the final draft - the fact that the work evolved significantly from the first draft is due in no small part to Behrooz and his feedback in between. Moreover, Behrooz modified the model code in ways that made these analyses at all possible. Thank you, Aiko and Behrooz, for all the time you've invested in me!

I also want to thank Dorian, who has been my informal contact in my master thesis struggles. He was not only a constant advisor on figure design or text versions but also always my go-to person when things weren't going so well. Anyway, coffee with Dorian fixed most of the motivation lows.

Furthermore, I want to thank the institute and especially Manfred Dorninger and Leopold Haimberger. The two of them had the difficult task of handling practically all of the teaching on their own in the last few years. This must have been very stressful, but I for one can say that I learned a lot and even exam situations were very pleasant.

However, I spent most of my study hours not at the Meteorology department, but at the Physics faculty on the 5th floor. There I did homework, wrote protocols, studied until my head was spinning, but most of all laughed a lot. Ben, Michi, Dorian, Luca, Philipp, Sophie, Leonie, Beate, Gregor, Herbert, Eva, Max, and Matti will always be part of my fondest study memories and many of them have developed from fellow students to my closest friends. Without you, studying would have been half the fun and definitely less doable!

Last but not least, I would like to thank my family, who has always supported me - far beyond financial support. Because of you, I could fully concentrate on my studies (and all the side-projects that I could never say no to) without having to worry about the serious side of life. Thank you for making this possible for me!